Multiscale Finite Volume Method for Coupled Single-Phase Flow and Heat Equations in Fractured Porous Media: Application to Geothermal Systems

Technische Universiteit Delft

Timothy Praditia
Student ID: 4492048

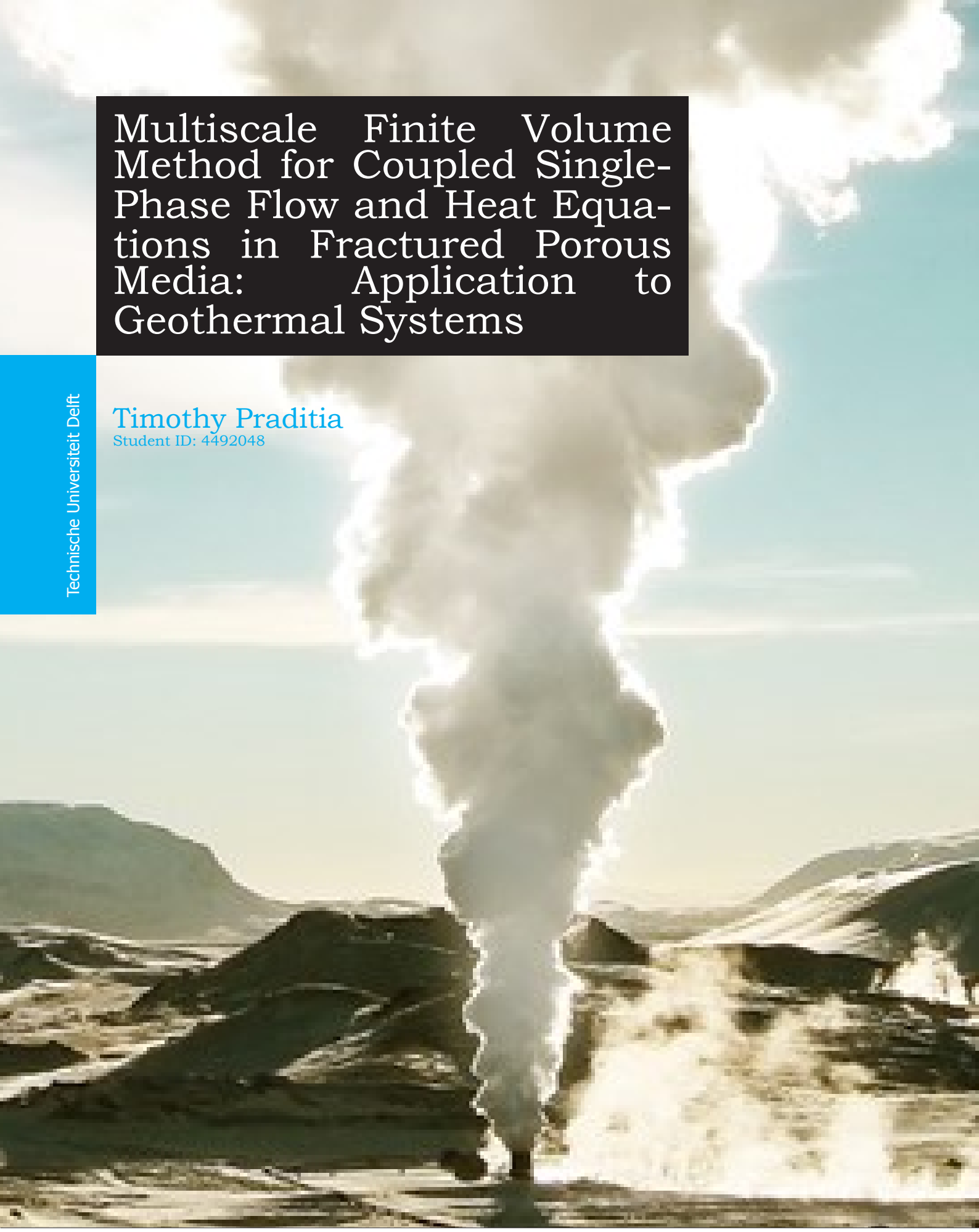

TU Delft Delft University of Technology

Challenge the future

Multiscale Finite Volume Method for Coupled Single-Phase Flow and Heat Equations in Fractured Porous Media: Application to Geothermal Systems

by

Timothy Praditia
Student ID: 4492048

in partial fulfillment of the requirements for the degree of

Master of Science
in Applied Earth Sciences

at the Delft University of Technology,
to be defended publicly on Tuesday August 29, 2017 at 10:00 AM.

Supervisor:	Dr. H. Hajibeygi,	TU Delft
Co-supervisor:	Prof. Dr.-Ing. R. Helmig,	Universität Stuttgart
Thesis committee:	Dr. D. Voskov,	TU Delft
	Prof. Dr. Ir. J. D. Jansen,	TU Delft
	Dr. Ir. F. P. van der Meer,	TU Delft

This thesis was conducted at Delft Advanced Reservoir Simulation (DARSim) group and part of Stuttgart Research Partnership-iNterdisciplinary Union of Porous media research at the University of Stuttgart (SRP NUPUS).

Cover photo taken from: http://www.mannvit.com/services/geothermal-energy/

An electronic version of this thesis is available at http://repository.tudelft.nl/.

TU Delft Delft University of Technology

Abstract

Modern geoscience challenges motivate the development of advanced simulation methods for large-scale geothermal fields, where single- or multi-phase flow is coupled with heat transfer equation in heterogeneous fractured formations. The state-of-the-art multiscale formulation for fractured media (F-AMS [1]) develops an efficient approach for flow equation only.

Here, for the first time, the F-AMS formulation is extended to coupled flow-heat equations arising from single-phase flow in fractured geothermal reservoirs. To this end, the multiscale operator is obtained based on elliptic basis functions for both pressure and temperature, to preserve the simplicity and efficiency of the method. ILU(0) 2^{nd} stage smoother is then used to guarantee convergence to any desired accuracy. Numerical results are presented to systematically analyse our multiscale approximate solutions compared with the fine scale ones for many challenging cases, including the outcrop-based geological fractured field. These results show that the developed multiscale formulation casts a promising framework for the real-field enhanced geothermal formations.

Acknowledgments

Working on a Master's thesis project is nowhere close to easy. Without support from many colleagues, friends, and family members, it might be impossible to finish it in time. Therefore, I would like to dedicate this part especially for people contributing to the finalisation of my thesis project.

I would like to thank Dr. Hadi Hajibeygi for being an inspiration ever since I attended his course of Rock Fluid Physics and especially Reservoir Simulation, and for all his guidance and suggestions throughout my study. He always tries to dedicate his time for his students no matter how busy he is. He is also one of the responsible people for making my three months exchange to the University of Stuttgart possible.

I also would like to thank Matei Ţene, for being available to have fruitful discussions regarding my project. My project is based on several of his works and publications.

I would like to thank the Department of Hydromechanics and Modelling of Hydrosystems at the University of Stuttgart as well, especially Prof. Dr.-Ing. Rainer Helmig and Dennis Gläser for their hospitality. They have been a very good host, helping me to get settled in Stuttgart. I would like to thank them for the discussions that we had, as well as the other fun stuffs.

I would like to thank the member of DARSim, for the regular presentations that we have and for the inputs given to my project. In particular, I would like to thank Matteo Cusini for his help in improving my code implementation, and Mousa HosseiniMehr for providing his fracture generation code, without which I would have spent a lot more time working on it myself.

I would also like to thank The Indonesian Endowment Fund for Education (Lembaga Pengelola Dana Pendidikan) for the financial support through the scholarship given to me during my whole study at TU Delft, from August 2015 - August 2017, as well as SRP NUPUS for granting me the opportunity to do part of my thesis project at the University of Stuttgart.

Last but not least, I would like to thank all of my family members and friends - whose names I could not mention one by one - for the moral support, without whom studying at TU Delft for 2 years would not have been as fun and memorable.

Timothy Praditia
22 August 2017, Delft

Contents

List of Figures

List of Tables

1

Introduction

Climate change nowadays has become one of the most discussed subjects of global concern. The United Nations Framework Convention on Climate Change (UNFCCC) has initiated the Paris Agreement in 2015 to hold the global average temperature increase well below 2°C, setting 1.5°C as the goal [5]. One way to reach this objective is to limit or reduce the global CO_2 emissions.

A major part of the CO_2 in the environment has come (and still is coming) from fossil fuel combustion to generate energy [6]. This implores us – as geoscientists – to accelerate the shift to cleaner energy resources (i.e. renewable energy).

Amongst the renewable energy sources, development of geothermal energy is relatively slow, even though the first power generation from geothermal energy commenced at 1904 in Larderello, Italy [7]. Geothermal has a lot of potentials to be developed even further because of its advantage over other renewable energy sources, thanks to its relatively steady energy supply.

According to the Geothermal Energy Association (GEA), because of the limited knowledge and technology in the geology and reservoir engineering, only 6-7% of the global geothermal potential is utilised [8]. The limited understanding of geothermal subsurface system also prevents optimised energy production, and therefore many geothermal projects are uneconomic because they could not pay out the high investment cost. A proper reservoir modelling and simulation could be used as the tool to improve subsurface understanding of the geothermal reservoirs.

The most important factors in reservoir numerical modelling are the accuracy of the models (i.e. fluid and rock properties as well as the physics) and efficiency of the simulation. Oftentimes, these factors have an inverse relationship. Highly accurate model usually leads to high computational cost, and vice versa. Multiscale simulation is proposed to be a state-of-the-art solution to this issue. Therefore, this study focuses on formulating accurate physics for coupled pressure and temperature calculation in single-phase geothermal reservoirs, as well as the implementation of multiscale method to improve the overall computational efficiency while maintaining the accuracy.

1.1. Fractured Geothermal Reservoirs

A natural geothermal system exploitation needs three key factors: heat, fluid (water and/or steam), and permeability. There are limited amount of places that are geologically viable to produce economic geothermal energy [9]. The main reason is the limited permeability in many potential geothermal fields leading to low production rates. One of the keys to increase production rate is by exploiting the fractures in the reservoir, because fractures act as highly conductive media, with the permeability usually orders of magnitude higher than the matrix permeability.

For geothermal reservoirs that are not naturally fractured, the concept of Enhanced Geothermal Systems (EGS) is introduced. EGS is considered for geothermal systems that have a high potential of heat generation, but with extremely low or no permeability due to their rock formation properties. Therefore, to be able to economically extract the heat, fracture networks are necessary and, therefore, are either generated or activated.

With the major role of fractures in flow and transport characteristics, the demand for accurate understanding of the coupled mass-heat transfer inside fractured reservoirs is becoming more and

more significant. This thesis work is the first step towards full multiscale simulation of geothermal fields, where a multiscale system is governed for a single-phase fluid flow coupled with heat transfer in fractured domains. Increasing geothermal power generation from fractured geothermal reservoirs – including EGS – could lead to unlocking those 93-94% untouched geothermal potential.

1.2. State-of-the-Art Simulation Aspects

In reservoir modelling, accurate consideration of the physical process and efficient simulation strategy are crucially important. In fractured reservoirs, the physics involve calculation of pressure and temperature in a coupled matrix-fracture system, where explicit consideration of fractures lead to more reliable simulations. With the increasing complexity and size of the physical model, multiscale simulation methods are required to be developed to improve the efficiency of the reservoir simulation with controllable required accuracy. In this section, the state-of-the-art simulation approaches related to embedded discrete fracture modelling approach and multiscale simulation are revisited, serving as foundations for this study.

1.2.1. Fracture Modelling

Modelling of fluid flow in fractured reservoirs brings additional complexity, mainly due to the difference in the scale of the flow conduits and possibility of extreme permeability contrasts between the matrix and fracture. Many studies have incorporated the existence of fractures in the reservoir model. One of the earliest works is a dual-porosity approach [10]. In this approach, the reservoir is modelled as having two continua: matrix and fractures. The matrix is assumed to have high contribution to the pore volume (primary porosity), but a low contribution to the flow capacity; and, vice versa, the opposite is considered for the contribution of the fractures (secondary porosity). An illustration of the dual-porosity approach is shown in figure 1.1.

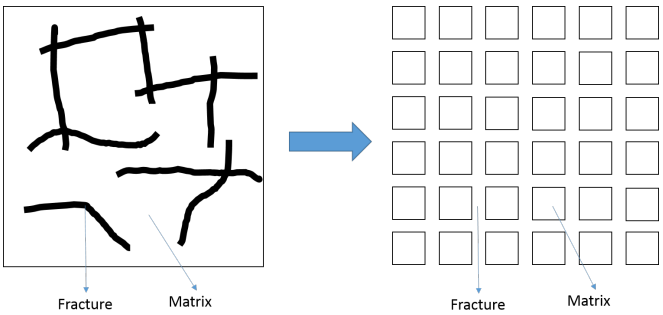

Figure 1.1: Illustration of dual-porosity reservoir model.

The dual-porosity method is beneficial in terms of its simplified model geometry and hence, efficient applications. However, the over-simplifications of the model, such as homogenisation of the matrix cells and the simplified geometry of the fracture networks lead to less accurate results [11].

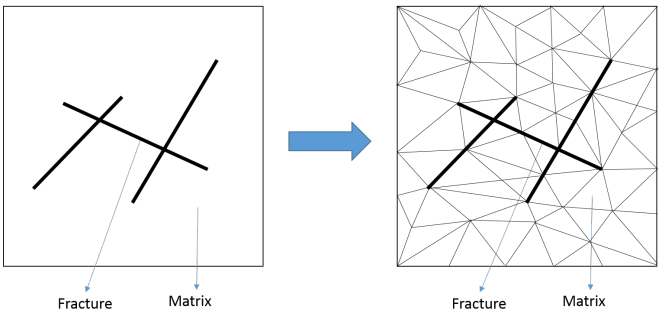

Figure 1.2: Illustration of unstructured grid model for DFM application.

An alternative approach is developed by explicitly accounting for lower-dimensional fractures using unstructured grids, with fractures being confined at the matrix grid interfaces. This model is referred

to as the Discrete Fracture Model (DFM) [11], and illustrated in figure 1.2. DFM has been proven to provide more accurate simulation results compared to dual-porosity model because of its capability to accurately capture the transfer of mass or heat between the matrix and fractures based on the fracture geometry. However, the main disadvantage of this approach is the use of unstructured grid, which makes the discretisation more complex and not very flexible. Specially, for reservoirs with dynamic fractures in 3D complex geometrical networks, this method becomes inefficient because the grid needs to be updated to adapt with the fracture geometry and possibly imposing very small-scale grids.

An alternative DFM method is developed to allow for independent matrix and fracture grids. This method is called Embedded Discrete Fracture Model (EDFM) [2, 12–16], which allows the matrix and fracture domain to be discretised on structured grids independent from each other, with a reasonably accurate coupling formulation between both domains, non-zeros only in the cells that are highlighted grey in figure 1.3. This approach assumes that the discrete fracture networks are embedded into the matrix cells, with a connectivity index that is calculated based on the average distance between matrix and fracture cell and the fracture surface area, to model the mass exchange between matrix and fracture [12].

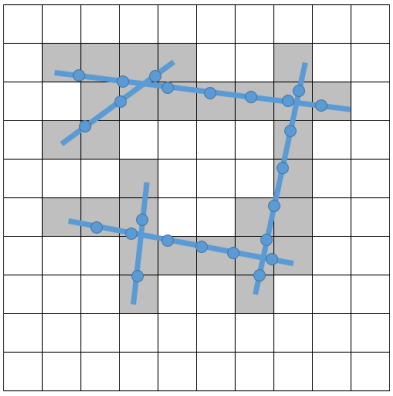

Figure 1.3: EDFM grid example, with the blue line representing the fractures, and the shaded grey areas are matrix cells that have coupling with fractures.

EDFM approach provides relatively simple coupling term between matrix and fracture domain, as well as flexibility in regards to fracture geometry and discretisation strategy. The simple coupling between matrix and fracture also benefits the multiscale simulation. As such, EDFM is being used in this thesis to model lower-dimensional fractures.

1.2.2. Multiscale Method

Simulation of geothermal reservoirs requires (at the very least) calculation of pressure and temperature at large scales with heterogeneous parameters. Both pressure and temperature are global parameters, meaning that changing the parameters at one cell can result in the change of the solution everywhere in the domain. Calculations of global parameters are known to be more expensive and time-consuming. For actual field-scale reservoir simulation, which can extend to many kilometers, the accuracy of the simulations is limited mainly by computational time and capacity of the computers. Upscaling is thus performed typically to have a reasonable computational time, at the expense of losing accuracy in the simulation results. Especially for fractured reservoirs, the reliability of excessively upscaled models is questionable.

To tackle this challenge, multiscale method is developed and extended through several studies in the literature. This method is an elegant way of constructing accurate coarse-scale systems with honoring fine-scale heterogeneity, the solutions of which are mapped back into fine scale to preserve the accuracy [17–20].

Among many developments, multiscale methods have been also extended to include compressible flows [18, 21]. These extensions differ from each other in the way the local basis functions are constructed (i.e., compressible or incompressible) and in the choice of second-stage smoother [20]. The state-of-the-art multiscale formulation for compressible systems (C-AMS) provides a convenient and flexible approach which is also being benchmarked against commercial simulators [22]. C-AMS sug-

gests that for compressible systems, elliptic (incompressible) local basis functions are overall superior to all many other choices, when computational efficiency for large-scale dynamic systems is considered. As such, C-AMS generates the full compressible system at the coarse scale, while interpolates its solution using incompressible basis functions. The high-frequency errors are reduced by ILU(0) as the 2^{nd} stage smoother [22].

For coupled matrix-fracture systems, the state-of-the-art multiscale approach, i.e., F-AMS, develops a fully flexible coupling strategy from decoupled, partially-coupled, to fully coupled framework [1]. Together with C-AMS, F-AMS serves as the foundation of this study. Here, for the first time, the F-AMS is being extended for coupled mass-heat transfer in single-fluid-phase fractured media. In this study, Multiscale Finite Volume (MSFV) framework is used due to its local mass conservation.

1.3. Research Goals

EDFM and multiscale methods have been well developed for pressure calculation. In geothermal reservoir simulations, formulation of EDFM and multiscale method (F-AMS) for temperature calculation and their implementation in simulators are also needed. Therefore, the main goals of this research are:

- Couple flow and heat equation for a single-phase water system in fractured geothermal reservoir.
- Formulate multiscale strategy for temperature calculation in fractured reservoir.
- Develop a simple fractured geothermal reservoir simulator from scratch to be used as proof-of-concept and to serve as the working prototype for the DARSim1 multiscale simulator, to be extended to include more complex physics (geomechanics, multi-phase, geochemistry, etc.) for real-field applications.

Stepwise, the development of this research started with understanding of the mass and energy balance equations for fractured reservoirs, discussed in chapter 2 and the numerical discretisation strategy including pressure and temperature coupling strategy which will be discussed in chapter 3. Then the multiscale strategy for both pressure and temperature calculation will be discussed in chapter 4, and the simulation results will be shown and discussed in chapter 5. The research will be concluded in chapter 6.

For this research, most of the MATLAB codes were developed by the author from scratch, except the codes for fracture generation and fracture properties calculation needed for the EDFM method which were taken from [23]. With the establishment of this simple simulator, as future work, it is desirable to continue the development by adding more complex physics and other improvements to make it more physically accurate and efficient.

2

Governing Equations

The simulator developed for this research is based on the conservation of mass and energy for single-phase flow in heterogeneous fractured porous media. Conservation of mass governs the pressure (flow) equation, and conservation of energy leads to the temperature (heat) equation. In this study, single-phase water is considered as the fluid, flowing through rocks with different geological properties and fracture networks.

This chapter discusses both conservation laws on coupled matrix-fracture system. The fundamental governing equations are explained in continuum form. The discretisation and coupling strategy for implementation in the simulator will be discussed in chapter 3.

2.1. Single-Phase Mass Conservation Equation

The mass conservation equation for single-phase water flow is written as

$$\frac{\partial}{\partial t}(\phi\rho_w) - \nabla \cdot (\rho_w \lambda_t \cdot \nabla p) = \rho_w q\,, \tag{2.1}$$

where ϕ denotes the porosity, ρ_w the water density, λ_t the water mobility, p the pressure, and q the volumetric flow rate or source term. In the equation, the gravity term is neglected for simplification. Mathematically, λ_t is defined as

$$\lambda_t = \lambda_w = \frac{k}{\mu_w}\,, \tag{2.2}$$

where k denotes the absolute permeability and is purely a rock property, and μ_w the water viscosity calculated using equation A.16. In fractures, permeability is calculated with a simple parallel plate model, and defined as [2]

$$k^f = \frac{a^2}{12}\,, \tag{2.3}$$

where a denotes the fracture aperture, which is the space between the two fracture plates. In real field, the aperture can change through out the fracture length, though in our test cases we have only considered constant values.

For coupled matrix-fracture systems, equation 2.1 is defined for both matrix and fracture domain, with an additional coupling term as flux exchange term between them. The extended mass balance equation reads

$$\left[\frac{\partial}{\partial t}(\phi\rho_w) - \nabla \cdot (\rho_w \lambda_t \nabla p)\right]^m = [\rho_w q]^{mw} + [\rho_w q]^{mf} \text{ on } \Omega^m \subset R^n\,, \tag{2.4}$$

for matrix, and

$$\left[\frac{\partial}{\partial t}(\phi\rho_w) - \nabla \cdot (\rho_w \lambda_t \nabla p)\right]^f = [\rho_w q]^{fw} + [\rho_w q]^{fm} \text{ on } \Omega^f \subset R^{n-1}\,, \tag{2.5}$$

for fracture, with superscript m denoting the matrix domain, f the fracture domain, and w for well. Note that the equation for fracture domain is defined in a lower dimensional space than the matrix [1].

The well volumetric flow rate, q^{mw} and q^{fw}, are calculated using Peaceman well model [24], i.e.,

$$q^{mw} = \frac{PI\ \lambda_t(p^w - p^m)}{V} = \beta^m(p^w - p^m), \tag{2.6}$$

for matrix, and

$$q^{fw} = \frac{PI\ \lambda_t(p^w - p^f)}{A} = \beta^f(p^w - p^f), \tag{2.7}$$

for fractures, where PI denotes the well productivity index, $\beta^m = \frac{PI\ \lambda_t}{V}$ and $\beta^f = \frac{PI\ \lambda_t}{A}$.

In equation 2.4 and 2.5, q^{mf} and q^{fm} are the volumetric flow rate between matrix and fracture, serving as the coupling term for both domain, and defined with

$$q^{mf} = \frac{CI\ \lambda^{f-m}(p^f - p^m)}{V} = \eta^m(p^f - p^m), \tag{2.8}$$

and

$$q^{fm} = \frac{CI\ \lambda^{f-m}(p^m - p^f)}{A} = \eta^f(p^m - p^f), \tag{2.9}$$

where CI is the connectivity index between matrix and fracture, $\eta^m = \frac{CI\ \lambda^{f-m}}{V}$ and $\eta^f = \frac{CI\ \lambda^{f-m}}{A}$, and λ^{f-m} is the effective mobility at matrix-fracture interface, calculated using harmonic average.

Note that the well flow rate, q^{mw} and the coupling term q^{mf} are normalised with the matrix volume. On the other hand, q^{fw} and q^{fm} are normalised with the fracture area to account for the different dimension at which matrix and fracture are defined. The normalisation will result in mass conservative coupling term when integrated, i.e.,

$$\int_V q^{mf} dV = -\int_A q^{fm} dA. \tag{2.10}$$

2.2. Single-Phase Energy Conservation Equation

In this study, local thermal equilibrium between fluid and solid is assumed [25, 26], meaning that the rock and the fluid have the same temperature at any given location. This assumption might not be valid for systems with relatively high fluid velocities compared with the conduction time-scale which is needed for the equilibrium to happen [27]. Consideration of local thermal non-equilibrium is out of the scope of this research, but should be considered in future research.

The single-phase energy conservation equation assuming local thermal equilibrium is written as [25]

$$\frac{\partial}{\partial t}(\phi\rho_w u_w + (1-\phi)\rho_r C_{pr} T) + \nabla \cdot (u_t h_w) - \nabla \cdot (\lambda_c \cdot \nabla T) = q_H, \tag{2.11}$$

where subscript r denotes rock properties, u_w and h_w the water specific internal energy and specific enthalpy, respectively, C_{pr} the rock specific heat, T the temperature, u_t the Darcy mass flow rate, λ_c the average thermal conductivity, and q_H the energy flow rate or source term.

Because local thermal equilibrium is assumed, the average thermal conductivity is calculated using volume weighted average between water and rock thermal conductivity, i.e.,

$$\lambda_c = \phi\lambda_{cw} + (1-\phi)\lambda_{cr}. \tag{2.12}$$

In equation 2.11, the mass flow rate u_t is calculated using pressure gradient obtained from the mass balance equation,

$$u_t = -\rho_w \lambda_t \cdot \nabla p. \tag{2.13}$$

For coupled matrix-fracture systems, equation 2.11 is extended also with a coupling term between both domains, written as

$$\left[\frac{\partial}{\partial t}(\phi\rho_w u_w + (1-\phi)\rho_r C_{pr} T) + \nabla\cdot(u_t h_w) - \nabla\cdot(\lambda_c\cdot\nabla T)\right]^m = [q_c]^{mf} + [q_H]^{mf} + [q_H]^{mw} \text{ on } \Omega^m \subset R^n, \tag{2.14}$$

for matrix domain, and

$$\left[\frac{\partial}{\partial t}(\phi\rho_w u_w + (1-\phi)\rho_r C_{pr} T) + \nabla\cdot(u_t h_w) - \nabla\cdot(\lambda_c\cdot\nabla T)\right]^f = [q_c]^{fm} + [q_H]^{fm} + [q_H]^{fw} \text{ on } \Omega^f \subset R^{n-1}, \tag{2.15}$$

for fracture domain, with superscript m denoting the matrix domain, f the fracture domain, and w for well.

The well source term is defined as the product of mass flow rate and specific enthalpy of the fluid,

$$q_H^{*w} = [\rho_w q h_w]^{*w}, \tag{2.16}$$

with $q_H^{*w} \in \{q_H^{mw}, q_H^{fw}\}$, and q^{*w} is the volumetric well flow rate defined in equation 2.6 and 2.7.

In equation 2.14 and 2.15, the coupling between matrix and fracture is divided into two parts: conduction and convection. The conduction coupling term q_c^{mf} and q_c^{fm} are defined analogous to the matrix-fracture mass transfer, written as

$$q_c^{mf} = \frac{CI\lambda_c^{f-m}(T^f - T^m)}{V} = \eta_c^m(T^f - T^m), \tag{2.17}$$

and

$$q_c^{fm} = \frac{CI\lambda_c^{f-m}(T^m - T^f)}{A} = \eta_c^f(T^m - T^f), \tag{2.18}$$

where the connectivity index CI used is the same with the CI used in equation 2.8 and 2.9, $\eta_c^m = \frac{CI\ \lambda_c^{f-m}}{V}$, and $\eta_c^f = \frac{CI\ \lambda_c^{f-m}}{A}$. The convection coupling term, q_H^{mf} and q_H^{fm}, are defined with

$$q_H^{mf} = [\rho_w q h_w]^{mf}, \tag{2.19}$$

and

$$q_H^{fm} = [\rho_w q h_w]^{fm}. \tag{2.20}$$

Note that the convection coupling term is analogous to the well source term defined in equation 2.16. These convection and conduction heat transfer between matrix and fracture will also result in energy conservation when integrated.

3

Fine Scale Discretisation and Coupling Strategy

The discrete form of equations 2.4, 2.5, 2.14, and 2.15 as well as the coupling strategy are presented in this chapter.

3.1. Fine Scale Discrete System

In this research, the discretisation scheme that will be used for the fine scale model is finite volume for the spatial discretisation and Euler backward (implicit) method for the time discretisation. This section explains about the linearisation of the conservation equations, as well as the connectivities used in the coupling of different domains (i.e. matrix, fractures, wells).

3.1.1. Mass Balance Discretisation

Linearisation

Using Euler backward method, all the unknown parameters are evaluated at time step $n+1$, and therefore, equation 2.4 and 2.5 are re-written as

$$\left[\frac{\phi^{n+1}}{\Delta t} - \frac{\phi^n \rho_w^n}{\rho_w^{n+1}\Delta t} - \frac{1}{\rho_w^{n+1}}\nabla\cdot(\rho_w \lambda_t \nabla p)^{n+1}\right]^* = q^{*w} + q^{*\bullet}, \tag{3.1}$$

where $q^{*w} \in \{q^{mw}, q^{fw}\}$ and $q^{*\bullet} \in \{q^{mf}, q^{fm}\}$. Notice that equation 3.1 is the result of dividing equation 2.4 and 2.5 with ρ_w^{n+1}.

Due to the non-linearity caused by the density and the porosity (in a compressible rock system), a linearisation scheme is needed. With Newton linearisation lemma applied, variables at $n+1$ are approximated with values at $\nu+1$, with ν denoting known values from previous iteration stage, and $\nu+1$ the unknown values that are calculated at the current iteration stage, i.e.,

$$\phi^{n+1} \approx \phi^{\nu+1} = \phi^{\nu} + \left.\frac{\partial\phi}{\partial p}\right|^{\nu}(p^{\nu+1} - p^{\nu}), \tag{3.2}$$

$$\left(\frac{1}{\rho_w}\right)^{n+1} \approx \left(\frac{1}{\rho_w}\right)^{\nu+1} = \left(\frac{1}{\rho_w}\right)^{\nu} + \left.\frac{\partial\left(\frac{1}{\rho_w}\right)}{\partial p}\right|^{\nu}(p^{\nu+1} - p^{\nu}), \text{ and} \tag{3.3}$$

$$p^{n+1} \approx p^{\nu+1}. \tag{3.4}$$

When convergence is reached, values at ν are equal to values at $\nu+1$ and $n+1$, due to the fact that $(p^{\nu+1} - p^{\nu}) = 0$. Substituting equation 3.2, 3.3, and 3.4 into equation 3.1, as well as expanding

$q^{*\bullet}$ using equation 2.8 and 2.9, and q^{*w} using equation 2.6 and 2.7 results in

$$\frac{C_p^\nu}{\Delta t}p^{*,\nu+1} - \frac{1}{\rho_w^\nu}\nabla\cdot(\rho_w^\nu\lambda_t\nabla p^{*,\nu+1}) + \beta^*(p^{*,\nu+1} - p^{w,\nu+1}) + \eta^*(p^{*,\nu+1} - p^{\bullet,\nu+1}) = RHS_p^\nu + \frac{C_p^\nu}{\Delta t}p^{*,\nu}, \quad (3.5)$$

where C_p^ν is defined as

$$C_p^\nu = \frac{\partial\phi}{\partial p}\bigg|^\nu - \phi^n\rho_w^n\frac{\partial\left(\frac{1}{\rho_w}\right)}{\partial p}\bigg|^\nu, \quad (3.6)$$

and RHS_p^ν is defined as

$$RHS_p^\nu = -\frac{\phi^\nu}{\Delta t} + \frac{\phi^n\rho_w^n}{\Delta t}\frac{1}{\rho_w^\nu}. \quad (3.7)$$

Note that in the diffusive term, the density is still defined at ν, in order to preserve the linearity of the discretised equation. Using finite volume discretisation, equation 3.5 is integrated over the control volume,

$$\begin{aligned}\int_\Omega\left(\frac{C_p^\nu}{\Delta t}p^{*,\nu+1}\right)d\Omega - \int_\Omega\left(\frac{1}{\rho_w^\nu}\nabla\cdot(\rho_w^\nu\lambda_t\nabla p^{*,\nu+1})\right)d\Omega + \int_\Omega\beta^*\left(p^{*,\nu+1} - p^{w,\nu+1}\right)d\Omega \\ + \int_\Omega\eta^*\left(p^{*,\nu+1} - p^{\bullet,\nu+1}\right)d\Omega = \int_\Omega\left(RHS_p^\nu + \frac{C_p^\nu}{\Delta t}p^{*,\nu}\right)d\Omega,\end{aligned} \quad (3.8)$$

with the diffusive term re-written using Gauss divergence theorem for a computational element Ω, i.e.,

$$-\int_\Omega\left(\frac{1}{\rho_w^\nu}\nabla\cdot(\rho_w^\nu\lambda_t\nabla p^{*,\nu+1})\right)d\Omega = -\frac{1}{\rho_w^\nu}\oint_\Gamma\left(\rho_w^\nu\lambda_t\nabla p^{*,\nu+1}\right)\cdot\tilde{\boldsymbol{n}}\,d\Gamma, \quad (3.9)$$

which is the net influx across the surface of the element. Algebraically, equation 3.8 can be written as

$$\boldsymbol{A}_p^\nu\cdot\boldsymbol{p}^{\nu+1} = \boldsymbol{f}_p^\nu, \quad (3.10)$$

or in expanded form,

$$\begin{bmatrix}\boldsymbol{A}_p^{mm} & \boldsymbol{A}_p^{mf} & \boldsymbol{A}_p^{mw}\\ \boldsymbol{A}_p^{fm} & \boldsymbol{A}_p^{ff} & \boldsymbol{A}_p^{fw}\\ \boldsymbol{A}_p^{wm} & \boldsymbol{A}_p^{wf} & \boldsymbol{A}_p^{ww}\end{bmatrix}^\nu\begin{bmatrix}\boldsymbol{p}^m\\ \boldsymbol{p}^f\\ \boldsymbol{p}^w\end{bmatrix}^{\nu+1} = \begin{bmatrix}\boldsymbol{f}_p^m\\ \boldsymbol{f}_p^f\\ \boldsymbol{f}_p^w\end{bmatrix}^\nu. \quad (3.11)$$

Connectivity Index

The coupling term between matrix and fracture domain is defined analogous to well source term. Instead of PI, a connectivity index CI is used to calculate equation 2.8 and 2.9, and in discrete form is defined as [12]

$$CI_{i-j} = \frac{A_{i-j}}{\langle d\rangle}, \quad (3.12)$$

where i denotes the fracture element, j the matrix element, and A_{i-j} the surface area of fracture element i that is connected with matrix j, and $\langle d\rangle$ is the average normal distance between the matrix and fracture. This variable has a dimension of length and due to its dependency on the fracture and matrix geometry, it is a grid dependent property.

The average distance $\langle d\rangle$ is calculated with [12]

$$\langle d\rangle = \frac{\int_V x_n(\boldsymbol{x}')d\boldsymbol{x}'}{V}, \quad (3.13)$$

where x_n is the distance between the matrix element and the fracture. Most of the times, $\langle d\rangle$ is calculated numerically, but for some cases, analytical solutions are available (see figure 3.1).

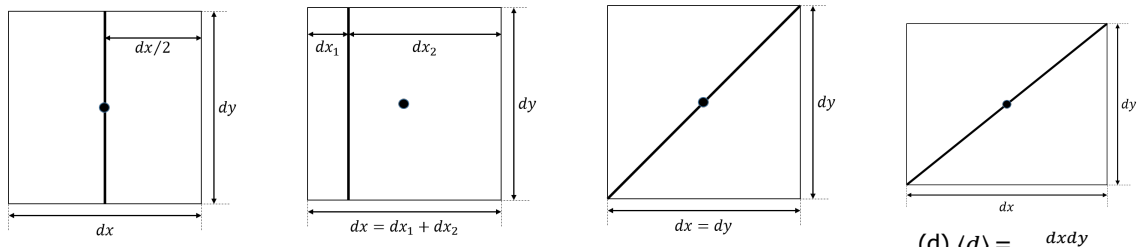

(a) $\langle d \rangle = \frac{dx}{4}$. (b) $\langle d \rangle = \frac{dx_1^2+dx_2^2}{2dx}$. (c) $\langle d \rangle = \frac{dx}{3\sqrt{2}}$. (d) $\langle d \rangle = \frac{dxdy}{3\sqrt{dx^2+dy^2}}$.

Figure 3.1: Examples of analytical solutions to calculate $\langle d \rangle$ in 2D [2].

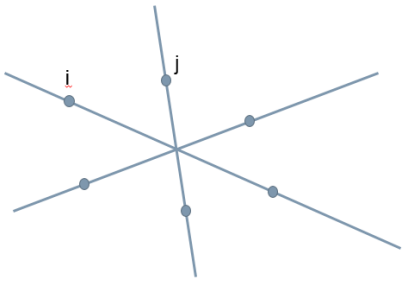

Figure 3.2: Illustration of fracture intersection.

Fracture Intersection

In fractured reservoirs, fracture networks can intersect each other. Therefore, a formulation is needed to calculate the connectivity between those networks. A "star-delta" transformation method adapted from electrical engineering field is introduced to calculate the transmissibility at fracture intersections [11].

Transmissibility between cell i and j in figure 3.2 is calculated by [11]

$$T_{ij} \approx \frac{\alpha_i \alpha_j}{\sum_{k=1}^{n} \alpha_k}, \tag{3.14}$$

where n is the number of connections in the intersection, and α_i is defined as

$$\alpha_i = \frac{A_i k_i}{D_i \mu_i}, \tag{3.15}$$

where A_i denotes the interface area of control volume i (in 2D problems, the fracture aperture of fracture element i), k_i the fracture permeability of cell i, D_i the distance between cell center i and the intersection, and μ_i the water viscosity at cell i.

3.1.2. Energy Balance Discretisation

Linearisation

Using Euler backward method, equation 2.14 and 2.15 are re-written as

$$\left[\frac{(\phi\rho_w u_w + (1-\phi)\rho_r C_{pr} T)^{n+1} - (\phi\rho_w u_w + (1-\phi)\rho_r C_{pr} T)^{n}}{\Delta t} + \nabla \cdot (u_t h_w)^{n+1} - \nabla \cdot (\lambda_c \cdot \nabla T)^{n+1}\right]^{*} = [q_c]^{*\bullet} + \left[(\rho_w q h_w)^{n+1}\right]^{*\bullet} + \left[(\rho_w q h_w)^{n+1}\right]^{*w}. \tag{3.16}$$

Due to the non-linearity caused by the specific internal energy and specific enthalpy, a linearisation

scheme is needed. With Newton linearisation lemma one obtains

$$u_w^{n+1} \approx u_w^{\nu+1} = u_w^{\nu} + \left.\frac{\partial u_w}{\partial T}\right|^{\nu} (T^{\nu+1} - T^{\nu}), \tag{3.17}$$

$$h_w^{n+1} \approx h_w^{\nu+1} = h_w^{\nu} + \left.\frac{\partial h_w}{\partial T}\right|^{\nu} (T^{\nu+1} - T^{\nu}), \text{ and} \tag{3.18}$$

$$T^{n+1} \approx T^{\nu+1}. \tag{3.19}$$

Substituting equation 3.17, 3.18, and 3.19 into equation 3.16 as well as expansion of the matrix-fracture coupling term results in

$$C_T^{\nu} T^{*,\nu+1} - \nabla \cdot (\lambda_c \nabla T^{*,\nu+1}) + \eta_c^* \left(T^{*,\nu+1} - T^{\bullet,\nu+1}\right) = RHS_T^{\nu} + C_T^{\nu} T^{*,\nu}, \tag{3.20}$$

where C_T^{ν} is defined as

$$C_T^{\nu} = \frac{\phi \rho_w^{\nu} \left.\frac{\partial u_w}{\partial T}\right|^{\nu} + (1-\phi)\rho_r C_{pr}}{\Delta t} + \nabla \cdot \left(u_t \left.\frac{\partial h_w}{\partial T}\right|^{\nu} \right) - \rho_w q^{*w} \left.\frac{\partial h_w}{\partial T}\right|^{\nu} - \rho_w q^{*\bullet} \left.\frac{\partial h_w}{\partial T}\right|^{\nu}, \tag{3.21}$$

and RHS_T^{ν} is defined as

$$RHS_T^{\nu} = -\frac{\phi(\rho_w^{\nu} u_w^{\nu} - \rho_w^{n} u_w^{n}) + (1-\phi)\rho_r C_{pr}(T^{\nu} - T^{n})}{\Delta t} - \nabla \cdot (u_t h_w^{\nu}) + [\rho_w q h_w^{\nu}]^{*w} + [\rho_w q h_w^{\nu}]^{*\bullet}. \tag{3.22}$$

Using finite volume discretisation, equation 3.20 is integrated over the control volume,

$$\begin{aligned} \int_{\Omega} \left(C_T^{\nu} T^{*,\nu+1}\right) d\Omega - \int_{\Omega} \left(\nabla \cdot (\lambda_c \nabla T^{*,\nu+1})\right) d\Omega + \int_{\Omega} \eta_c^* \left(T^{*,\nu+1} - T^{\bullet,\nu+1}\right) d\Omega \\ = \int_{\Omega} \left(RHS_T^{\nu} + C_T^{\nu} T^{*,\nu}\right) d\Omega, \end{aligned} \tag{3.23}$$

with the diffusive term re-written using Gauss divergence theorem for a computational element Ω, i.e.,

$$-\int_{\Omega} \left(\nabla \cdot (\lambda_c \nabla T^{*,\nu+1})\right) d\Omega = -\oint_{\Gamma} \left(\lambda_c \nabla T^{*,\nu+1}\right) \cdot \tilde{\boldsymbol{n}} \, d\Gamma, \tag{3.24}$$

which is the net influx integrated across the surface area of the flow.

The advective term is also re-written using Gauss divergence theorem as

$$\int_{\Omega} (\nabla \cdot (u_t h_w^{\nu})) \, d\Omega = \oint_{\Gamma} (u_t h_w^{\nu}) \cdot \tilde{\boldsymbol{n}} \, d\Gamma. \tag{3.25}$$

Algebraically, equation 3.23 can be written as

$$\boldsymbol{A}_T^{\nu} \cdot \boldsymbol{T}^{\nu+1} = \boldsymbol{f}_T^{\nu}, \tag{3.26}$$

or in expanded form,

$$\begin{bmatrix} \boldsymbol{A}_T^{mm} & \boldsymbol{A}_T^{mf} & \boldsymbol{A}_T^{mw} \\ \boldsymbol{A}_T^{fm} & \boldsymbol{A}_T^{ff} & \boldsymbol{A}_T^{fw} \\ \boldsymbol{A}_T^{wm} & \boldsymbol{A}_T^{wf} & \boldsymbol{A}_T^{ww} \end{bmatrix}^{\nu} \begin{bmatrix} \boldsymbol{T}^{m} \\ \boldsymbol{T}^{f} \\ \boldsymbol{T}^{w} \end{bmatrix}^{\nu+1} = \begin{bmatrix} \boldsymbol{f}_T^{m} \\ \boldsymbol{f}_T^{f} \\ \boldsymbol{f}_T^{w} \end{bmatrix}^{\nu}. \tag{3.27}$$

Note that in the injection well temperature contributes in the linear system calculation, while production well temperature is assumed to be equal to the grid block temperature at the well location. Moreover, the advective term in the energy balance equation, $\nabla \cdot (u_t h_w^{\nu})$, is calculated using an upwind method [26, 28]. In the upwind method, the enthalpy information upstream of the flow is used to define the value of the enthalpy at the interface (see figure 3.3).

Similarly, the well source term and the convection coupling term between matrix and fracture domain are calculated using an upwind scheme.

Fracture intersection for energy equation is being treated in a similar manner as for the flow, with the only addition that here – in energy equation – such a treatment is needed for both conduction and convection.

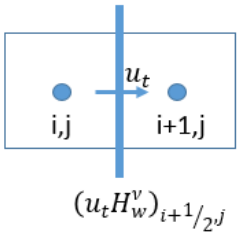

Figure 3.3: Schematic of energy balance advective term at the interface.

Boundary Conditioning

No-flow boundary condition is considered to be a reasonable assumption for pressure calculation. In temperature calculation, however, there might be some energy flowing into and/or out of the reservoir domain into the surrounding rocks. The average heat flux through the Earth's crust of approximately $59\ mW/m^2$ is implemented as one of the source terms of the energy balance equation [7]. This value can also be adjusted to model the reservoir in a more specific location that has a different heat flux value. Another heat flux occurring due to the temperature gradient with surrounding rocks could also be assigned at the reservoir boundaries as Neumann boundary condition to account for the heat supply or heat loss to the surroundings. A detailed heat flux modeling and formulation is outside the scope of this study, but carried out in a BSc thesis work [29] parallel to this MSc thesis work.

3.2. Coupling Strategy

Assuming that for the single-phase system of our concern, the coupling between the mass and heat transfer equation is not significant, a sequential implicit approach is being followed. As such, an outer loop iteration between pressure and temperature solver (see flowchart in figure 3.4) is needed to account for the co-dependency between both conservation equations. At the end of each outer loop, the convergence for both pressure and temperature are checked. If the system has reached convergence, meaning that both pressure and temperature change from the previous sequential iteration are below the pre-defined tolerance, then the simulation moves forward to the next time step. For multiphase problems with strong dependency of parameters to geochemical and geomechanical effects, one may need to consider a fully implicit coupling [30].

The sequential implicit algorithm is shown in figure 3.4. Note that in figure 3.4, ε_s is the tolerance used in the sequential outer loop. Also, figures 3.5 and 3.6 present the procedure for flow and temperature solver, respectively.

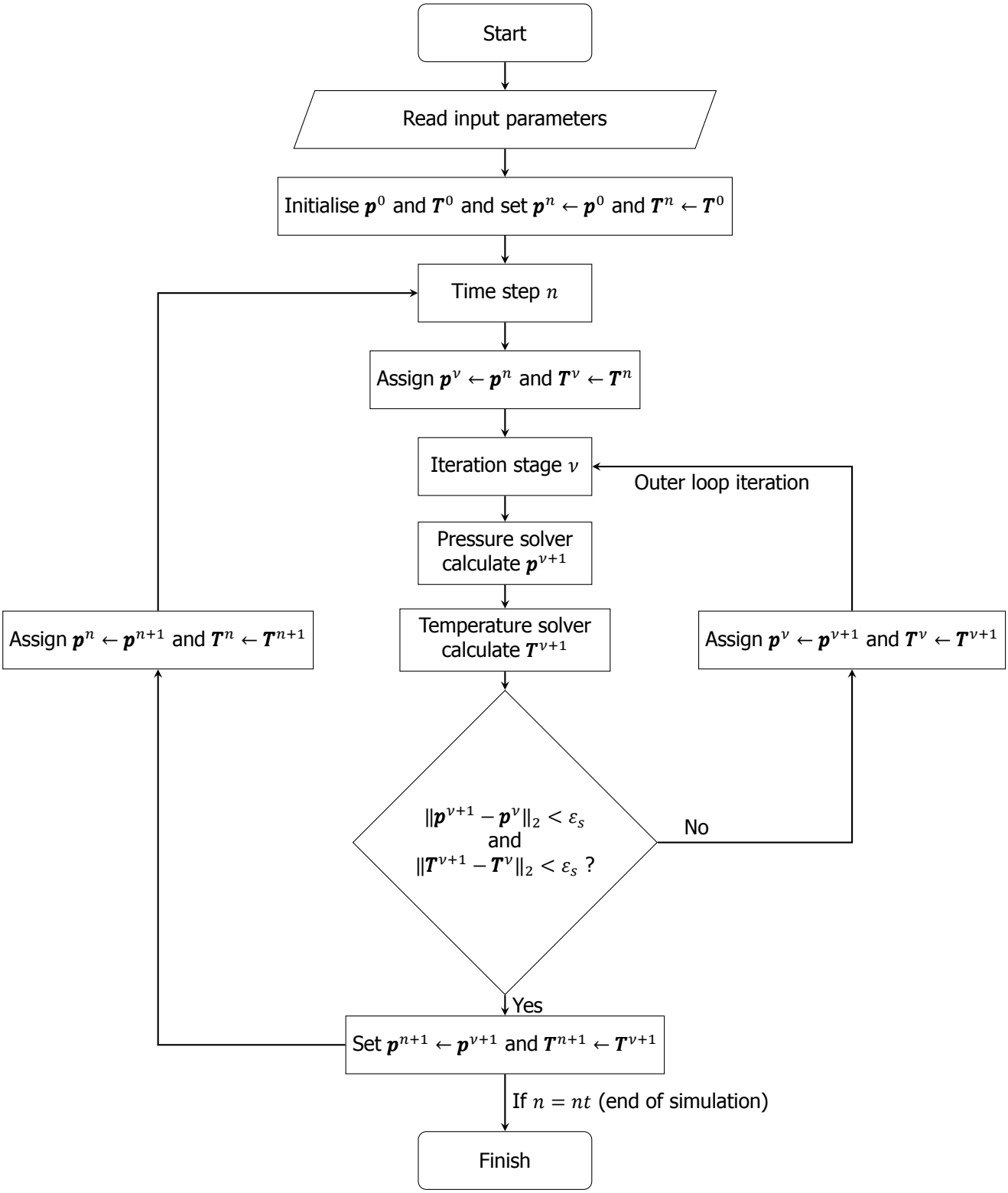

Figure 3.4: Flowchart of sequential implicit pressure and temperature solver.

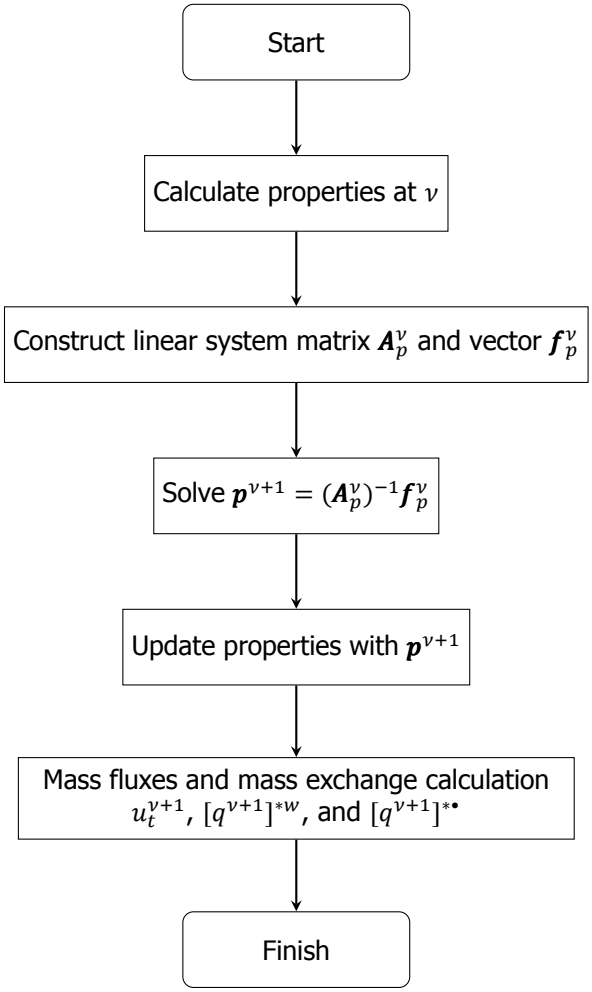

Figure 3.5: Flowchart of fine scale pressure solver.

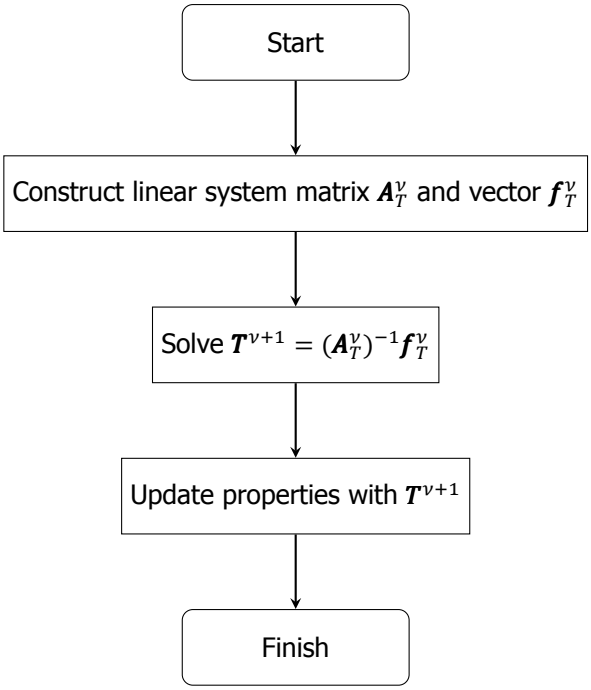

Figure 3.6: Flowchart of fine scale temperature solver.

4

Multiscale Method

Existence of fractures brings more degrees of freedom in the linear system and therefore increases the computational time (and costs). In field scale simulation, upscaling is usually conducted to reduce the problem size. In a conventional upscaling process, the averaging of the fine scale grid properties leads to loss of details, especially in heterogeneous reservoirs. Multiscale method, instead, provides a solution for this issue because it honors the fine-scale heterogeneity in the coarse-scale systems. It is also a unique method due to its feature that enables conversion of the coarse scale solution back to the fine scale, in a consistent and conservative manner, therefore providing solutions in both scales, hence the name "multiscale".

This chapter explains the multiscale method for both pressure and temperature calculation, starting from the construction of the multiscale grids, superposition of pressure and temperature, basis function formulation, the algebraic description, and the algorithm for its implementation in the simulator.

4.1. Multiscale Grids

The first step in multiscale method is the construction of the multiscale grids. Multiscale grids consist of primal and dual coarse grids and are imposed on the fine scale grids (see figure 4.1). The dual coarse grids (shaded orange, Ω^d, in figure 4.1) are overlapping with the other dual coarse grids, while the primal coarse grids (shaded green, Ω^c, in figure 4.1) are not. The primal coarse grids contain one coarse node each, while dual coarse grids are bounded by four coarse nodes (in 2D domain) in their corners, and therefore their edges are overlapping. Dual coarse grids are used to calculate local basis functions.

In figure 4.1, different colours are assigned to vertices, edges, and faces. These three elements are important for the localisation assumption. An element within a certain rank has connections only to other elements that are directly more superior or inferior. The ranks from highest to lowest are: vertices, edges, and faces. With these defined ranks, the basis function is solved first for the vertices defined by

$$\Phi_c^d(x_i) = \delta_{ci} = \begin{cases} 1, & \text{if } c = i \\ 0, & \text{if } c \neq i \end{cases}, \tag{4.1}$$

where c denotes the primal coarse grid, d the dual coarse grid, and x_i is one of the coarse node on the corner of the dual coarse grid. Then, the basis function is solved at the edges by assuming local 1D problem along them (no flux going in or out of the plane perpendicular to the edges), and finally the faces by using all the edges solution as Dirichlet boundary condition.

Figure 4.2 shows an example of embedded fracture networks on the matrix grid. The dark blue cells mark the vertices/coarse nodes of the matrix and fracture elements. For multiscale implementation, the main benefit of using EDFM is that the coarsening strategy of the fracture elements could be entirely independent of the matrix coarsening. Moreover, the fracture elements could be connected to every matrix cell, whether it is a vertex, edge, or face.

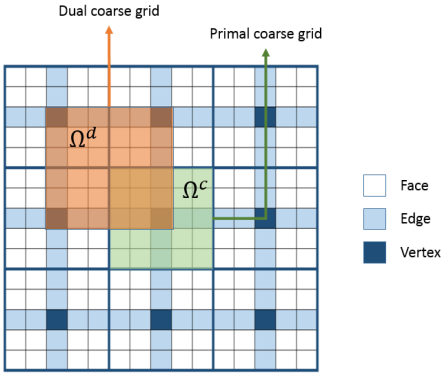

Figure 4.1: Multiscale grids in 2D with 15 x 15 fine cells and coarsening ratio of 5.

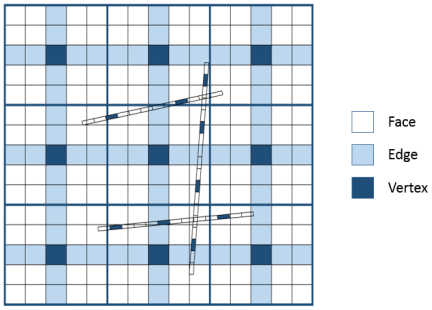

Figure 4.2: Multiscale grids in 2D matrix-fracture system.

4.2. Pressure Multiscale

In this section, the multiscale method for pressure calculation is explained, including the pressure approximation and basis function formulation.

4.2.1. Pressure Approximation

In F-AMS method, the fine scale solution is approximated based on superposition principle, defined with

$$p^m \approx p'^m = \sum_{i=1}^{N_{cm}} \Phi_i^{mm} \check{p}_i^m + \sum_{i=1}^{N_f} \sum_{j=1}^{N_{cf_i}} \Phi_j^{mf} \check{p}_j^{f_i} + \sum_{k=1}^{N_w} \Phi_k^{mw} \check{p}_k^w \,, \tag{4.2}$$

for matrix pressure, and

$$p^f \approx p'^f = \sum_{i=1}^{N_{cm}} \Phi_i^{fm} \check{p}_i^m + \sum_{i=1}^{N_f} \sum_{j=1}^{N_{cf_i}} \Phi_j^{ff} \check{p}_j^{f_i} + \sum_{k=1}^{N_w} \Phi_k^{fw} \check{p}_k^w \,, \tag{4.3}$$

for fracture pressure, where Φ^{m*} denotes basis functions in matrix domain, coupled with domain $*$ (i.e. matrix (m), fracture (f), or well (w)), Φ^{f*} the basis functions in fracture domain, coupled with domain $*$, N_{cm} the number of primal coarse cells in matrix domain, N_f the number of fracture networks, N_{cf_i} the number of primal coarse cell in fracture i, and N_w the number of wells.

4.2.2. Sub-methods of F-AMS

One of the reasons F-AMS is chosen for this study is that of its flexibility. The division of the prolongation operator into sub-matrices enables flexibility in choosing the coupling strategy. There are four different possibilities to include fracture coupling in F-AMS [1], namely, Decoupled-AMS, Frac-AMS, Rock-AMS, and Coupled-AMS.

Based on their names, Decoupled-AMS and Coupled-AMS can be easily defined. Decoupled-AMS formulates basis function without any coupling between matrix and fractures, resulting in $\boldsymbol{\mathcal{P}}^{mf} = 0$ and $\boldsymbol{\mathcal{P}}^{fm} = 0$. Coupled-AMS, on the other hand, is the opposite, resulting in fully coupled basis function formulation and therefore, $\boldsymbol{\mathcal{P}}^{mf}$ and $\boldsymbol{\mathcal{P}}^{fm}$ are both non-zero.

Frac-AMS and Rock-AMS are formulated with partial coupling between matrix and fractures. In Frac-AMS, basis function is formulated with the assumption that the matrix basis function is coupled with the fractures, but fracture basis function is decoupled from the matrix. On the other hand, Rock-AMS assumes that matrix basis function is fully decoupled with fractures, but fracture basis function is coupled with the matrix domain.

In this study, two of these sub-methods are considered: Decoupled-AMS due to its efficient setup and simple formulation, and Frac-AMS due to the assumption that the main heterogeneity contrast resulting from the fractures is emphasised. Rock-AMS and Coupled-AMS place more emphasis on matrix heterogeneity and therefore could be more suitable for highly heterogeneous matrix system.

The general formulation of the basis function is written as

$$-\nabla \cdot (\lambda_t^* \cdot \nabla \Phi^{*\bullet}) + \sum_{j \in conn_{mf}^*} \eta_j^* \xi(\Phi^{*\bullet}) + \sum_{j \in perf_w^*} \beta_j^* (\Phi^{*\bullet} - \Phi^{w\bullet}) = 0, \tag{4.4}$$

where $\Phi^{*\bullet} \in \{\Phi^{mm}, \Phi^{mf}, \Phi^{mw}, \Phi^{fm}, \Phi^{ff}, \Phi^{fw}\}$. The function $\xi(\Phi^{*\bullet})$ is different for each sub-method.

Equation 4.4 is formulated based on an equivalent incompressible system equation. This formulation is proven to be the most efficient strategy (based on CPU measurements) because it eliminates the need to frequently update the local basis function, while the fully compressible coarse-scale system takes care of the global compressibility effects [22].

Decoupled-AMS

In Decoupled-AMS, all basis functions are calculated independent of interactions with other domains, that is

$$\xi(\Phi^{*\bullet}) = 0 \ \forall \Phi^{*\bullet} \in \{\Phi^{mm}, \Phi^{mf}, \Phi^{mw}, \Phi^{fm}, \Phi^{ff}, \Phi^{fw}\}. \tag{4.5}$$

An example of the pressure basis function calculated using Decoupled-AMS approach is shown in figure 4.3. In figure 4.3a, it is shown that the matrix basis function is not affected by fracture existence, as well as fracture basis function not affected by matrix basis function in figure 4.3b. The basis function forms a partition of unity, meaning that the sum of all the basis function is equal to 1, as shown in figure 4.3c.

Frac-AMS

In Frac-AMS method, fracture basis function Φ^{ff} is first calculated, decoupled with the matrix basis function, using

$$\xi(\Phi^{ff}) = 0. \tag{4.6}$$

These values are then used as Dirichlet boundary condition to calculate Φ^{mf} and setting

$$\xi(\Phi^{mf}) = \Phi^{mf} - \Phi^{ff} \tag{4.7}$$

to account for the connectivity of matrix basis function with the fracture domain. An example is shown in figure 4.4a, where Φ^{ff} is plotted in the fractures and Φ^{mf} is plotted in the matrix with the coupling effect clearly observed.

The matrix basis function Φ^{mm} is calculated by setting

$$\xi(\Phi^{mm}) = \Phi^{mm}, \tag{4.8}$$

therefore also accounting for fracture existence. An example is shown in figure 4.4b where the fracture basis function Φ^{fm} is set to 0, and the matrix basis function Φ^{mm} observing the effect of the fracture existence, as though the fractures act as flow barriers. The beauty of F-AMS is that it always results in partition of unity, as shown in figure 4.4c for Frac-AMS approach.

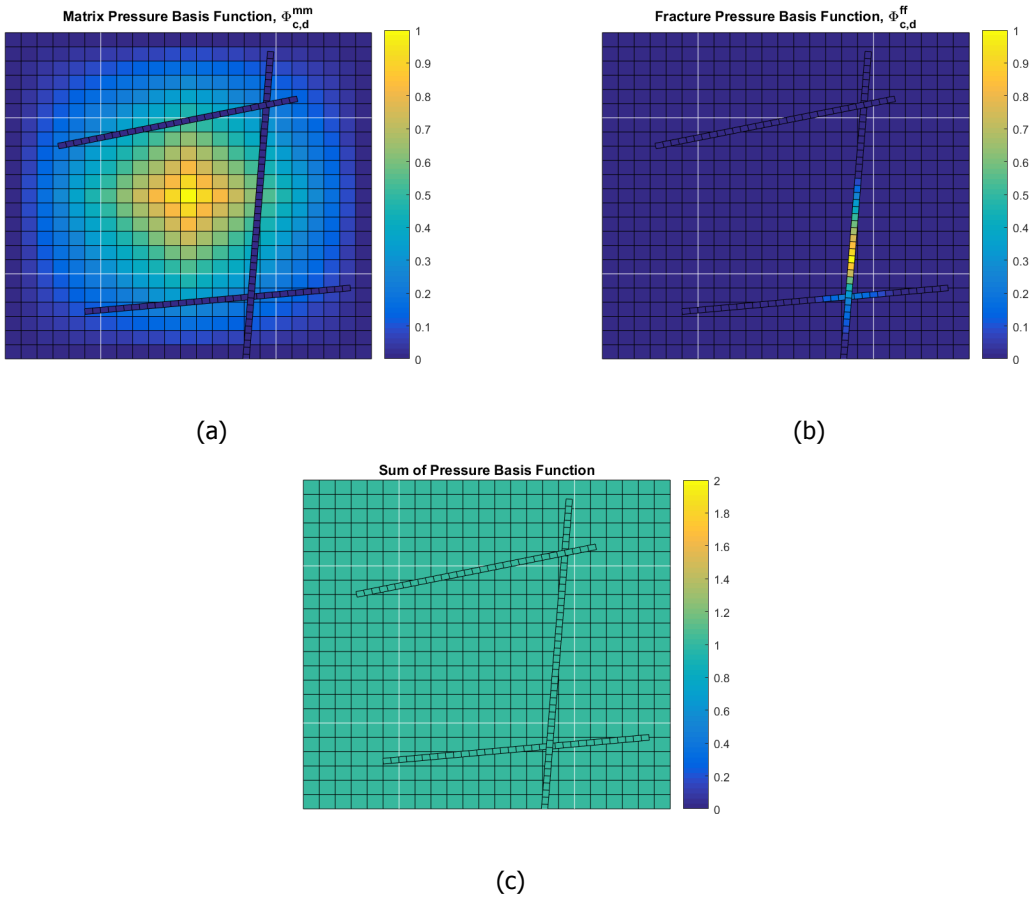

Figure 4.3: Matrix basis function $\Phi_{c,d}^{mm}$ (a), fracture basis function $\Phi_{c,d}^{ff}$ (b), and sum of basis functions (c) using Decoupled-AMS approach.

4.2.3. Fine Scale Flux Reconstruction

In the pressure multiscale method, one of the most important step is the fine scale flux reconstruction. In MSFV, the mass fluxes are conservative only in coarse scale because of the localisation assumption. Therefore, the fine scale fluxes need to be reconstructed if the solution is not converged to machine accuracy [1]. This is especially important in multiphase flows, to accurately predict the saturation front since the fractional flow is sensitive to the flux. In geothermal simulations, conservative mass flux is also needed in the energy balance calculation. Therefore, it is worth revisiting the fine scale flux reconstruction in this subsection.

The mass flow rate formulation

$$\boldsymbol{u}_t' = -\rho_w \lambda_c \cdot \nabla p' \tag{4.9}$$

is valid at the primal coarse cell boundaries $\partial\Omega_c$. The fine scale flux reconstruction can be achieved by calculating local pressure solution based on

$$[\frac{\partial}{\partial t}(\phi\rho_w) - \nabla\cdot(\rho_w\lambda_t\nabla p_c'')]^* = [\rho_w q]^{*w} + [\rho_w q]^{*\bullet} \text{ on } \Omega_c\,, \tag{4.10}$$

with the boundary condition

$$(\rho_w\lambda_t\nabla p_c'')\cdot\bar{\boldsymbol{n}}_c = (\rho_w\lambda_t\nabla p')\cdot\bar{\boldsymbol{n}}_c \text{ at } \partial\Omega_c\,, \tag{4.11}$$

where $\bar{\boldsymbol{n}}_c$ is the normal vector pointing out of the primal coarse cell boundaries, meaning that the fluxes at the coarse cell interfaces are used as Neumann boundary condition to calculate the reconstructed local pressure. The mass flow rate is then reconstructed with

$$\boldsymbol{u}_t'' = \begin{cases} -\rho_w\lambda_t\cdot\nabla p_c'', & \text{on } \Omega_c \\ -\rho_w\lambda_t\cdot\nabla p', & \text{at } \partial\Omega_c \end{cases}. \tag{4.12}$$

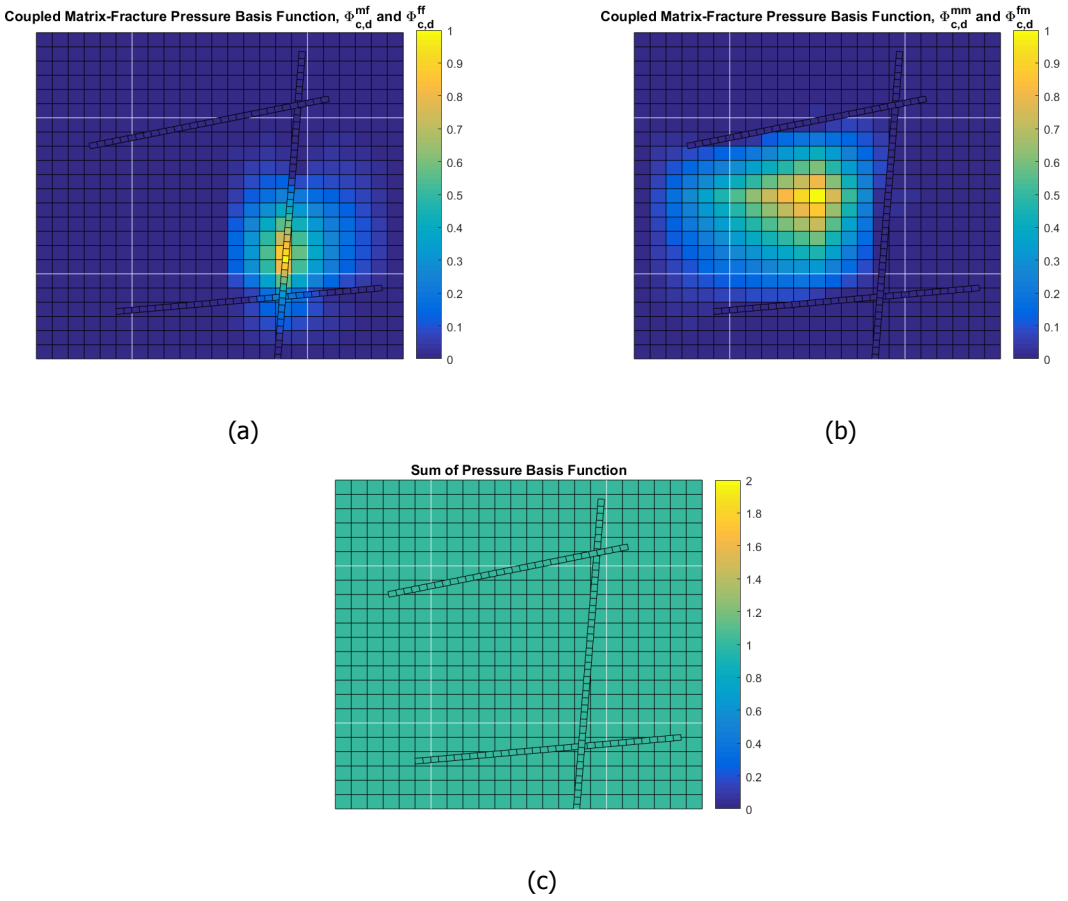

Figure 4.4: $\Phi^{mf}_{c,d}$ and $\Phi^{ff}_{c,d}$ (a), $\Phi^{mm}_{c,d}$ and $\Phi^{fm}_{c,d}$ (b), and sum of basis functions (c) using Frac-AMS approach.

4.3. Temperature Multiscale

4.3.1. Temperature Approximation

In this section, the multiscale method for temperature calculation is developed, based on an extension of the fine-scale temperature approximation as

$$T^m \approx T'^m = \sum_{i=1}^{N_{cm}} \Phi_i^{mm} \check{T}_i^m + \sum_{i=1}^{N_f} \sum_{j=1}^{N_{cf_i}} \Phi_j^{mf} \check{T}_j^{f_i} + \sum_{k=1}^{N_{w,inj}} \Phi_k^{mw} \check{T}_k^w \,, \tag{4.13}$$

for matrix, and

$$T^f \approx T'^f = \sum_{i=1}^{N_{cm}} \Phi_i^{fm} \check{T}_i^m + \sum_{i=1}^{N_f} \sum_{j=1}^{N_{cf_i}} \Phi_j^{ff} \check{T}_j^{f_i} + \sum_{k=1}^{N_{w,inj}} \Phi_k^{fw} \check{T}_k^w \,, \tag{4.14}$$

for fracture, where Φ^{m*} denotes basis functions in matrix domain, coupled with domain $*$ (e.g. matrix (m), fracture (f), or well (w)), Φ^{f*} the basis functions in fracture domain, coupled with domain $*$, N_{cm} the number of primal coarse cells in matrix domain, N_f the number of fracture networks, N_{cf_i} the number of primal coarse cell in fracture i, and $N_{w,inj}$ the number of injection wells.

4.3.2. Basis Function Formulation

In development of an efficient multiscale method, the proper choice of basis function formulation is important. The important factors to consider for basis functions are their accuracy in representation of the underlying heterogeneity (accuracy), and their independency on the primary unknowns for

adaptivity (efficiency). In this work, these aspects are being considered to formulate temperature basis functions. As such, In this work, the heat basis functions are formulated based on the conduction term within the whole energy balance equation. This allows for convenient implementation, as well as efficient algorithm (since basis functions are not required to be frequently updated).

To account for the fractures in the temperature basis functions, two types of matrix-fracture coupling formulations are considered: Decoupled-AMS and Frac-AMS. The general formulation of the temperature basis function can be defined as

$$-\nabla \cdot (\lambda_c^* \cdot \nabla \Phi^{*\bullet}) + \sum_{j \in conn_{mf}^*} \eta_{c,j}^* \xi(\Phi^{*\bullet}) = 0\,, \tag{4.15}$$

where $\Phi^{*\bullet} \in \{\Phi^{mm}, \Phi^{mf}, \Phi^{mw}, \Phi^{fm}, \Phi^{ff}, \Phi^{fw}\}$. The function $\xi(\Phi^{*\bullet})$ is different for each coupling approach, and is defined the same way as in pressure F-AMS method (see equation 4.5, 4.6, 4.7, and 4.8). Because the basis functions are only dependent on thermal conductivity λ_c, they do not need to be updated frequently. As will be seen in the result section, this formulation is shown to be working well to interpolate the coarse-scale temperature values to the fine scale. Note that these basis functions in combination of flow basis functions form the full prolongation (interpolation) operator to map between coarse and fine scale values for flow and heat.

Note that in equation 4.15, there is no coupling between reservoir and well. In pressure basis function, the coupling between matrix or fracture and well basis function can be easily calculated using Peaceman well model. In the energy balance equation, however, the coupling between well and reservoir temperature is done via enthalpy flow rate, and not directly with temperature.

Since the temperature basis function is formulated using similar formulation with pressure basis function, an example of the basis function would be the same as shown in figure 4.3 and 4.4.

4.4. Algebraic Description

In the multiscale method, there are two important operators, namely the prolongation $\mathcal{P}$ and the restriction $\mathcal{R}$ operator. The prolongation operator is a matrix constructed by the basis function values (interpolators) to map the coarse scale to fine scale solution. The restriction operator, on the other hand, is useful to map from fine scale to coarse scale. In finite-volume formulation, it acts as an integrator of all the fine scale fluxes, source/sink terms, as well as accumulation inside a primal coarse cell. In this section, the algebraic description is explained in a generic way for both pressure and temperature calculation. More specifically, the prolongation operator reads

$$\boldsymbol{\mathcal{P}} = \begin{bmatrix} \boldsymbol{\mathcal{P}}^m \\ \boldsymbol{\mathcal{P}}^f \\ \boldsymbol{\mathcal{P}}^w \end{bmatrix} = \begin{bmatrix} \boldsymbol{\mathcal{P}}^{mm} & \boldsymbol{\mathcal{P}}^{mf} & \boldsymbol{\mathcal{P}}^{mw} \\ \boldsymbol{\mathcal{P}}^{fm} & \boldsymbol{\mathcal{P}}^{ff} & \boldsymbol{\mathcal{P}}^{fw} \\ \boldsymbol{\mathcal{P}}^{wm} & \boldsymbol{\mathcal{P}}^{wf} & \boldsymbol{\mathcal{P}}^{ww} \end{bmatrix}, \tag{4.16}$$

where $\boldsymbol{\mathcal{P}}^m$ stores the matrix basis functions $\Phi_{c,d}^{m*}$, i.e.,

$$\boldsymbol{\mathcal{P}}^m = \left[\begin{array}{ccc|ccccccc|ccc} \vdots & \cdots & \vdots & \vdots & \cdots & \vdots & \cdots & \vdots & \cdots & \vdots & \vdots & \cdots & \vdots \\ \Phi_1^{mm} & \cdots & \Phi_{N_{cm}}^{mm} & \Phi_1^{mf_1} & \cdots & \Phi_{N_{cf_1}}^{mf_1} & \cdots & \Phi_1^{mf_{N_f}} & \cdots & \Phi_{N_{cf_{N_f}}}^{mf_{N_f}} & \Phi_1^{mw} & \cdots & \Phi_{N_w}^{mw} \\ \vdots & \cdots & \vdots & \vdots & \cdots & \vdots & \cdots & \vdots & \cdots & \vdots & \vdots & \cdots & \vdots \end{array}\right], \tag{4.17}$$

and $\boldsymbol{\mathcal{P}}^f$ stores the fracture basis functions $\Phi_{c,d}^{f*}$, i.e.,

$$\boldsymbol{\mathcal{P}}^f = \left[\begin{array}{ccc|ccccccc|ccc} \vdots & \cdots & \vdots & \vdots & \cdots & \vdots & \cdots & \vdots & \cdots & \vdots & \vdots & \cdots & \vdots \\ \Phi_1^{fm} & \cdots & \Phi_{N_{cm}}^{fm} & \Phi_1^{ff_1} & \cdots & \Phi_{N_{cf_1}}^{ff_1} & \cdots & \Phi_1^{ff_{N_f}} & \cdots & \Phi_{N_{cf_{N_f}}}^{ff_{N_f}} & \Phi_1^{fw} & \cdots & \Phi_{N_w}^{fw} \\ \vdots & \cdots & \vdots & \vdots & \cdots & \vdots & \cdots & \vdots & \cdots & \vdots & \vdots & \cdots & \vdots \end{array}\right]. \tag{4.18}$$

In non-fractured reservoirs, the sub-matrices $\boldsymbol{\mathcal{P}}^{f*}$ and $\boldsymbol{\mathcal{P}}^{*f}$ are zero matrices, therefore reducing the prolongation operator to only matrix and well domains. Note also that $\boldsymbol{\mathcal{P}}^{*w}$ for temperature calculation has the column size of $N_{w,inj}$, and $\boldsymbol{\mathcal{P}}^{w*}$ has the row size of $N_{w,inj}$ instead of N_w.

The MSFV restriction operator on structured grid is defined as

$$\boldsymbol{\mathcal{R}}_{i,j}^{FV} = \begin{cases} 1, & \text{if fine cell } j \text{ is contained in primal coarse cell } i \\ 0, & \text{otherwise} \end{cases}, \tag{4.19}$$

and in MSFE method, the restriction is defined as the transpose of the prolongation operator, $\boldsymbol{\mathcal{R}}^{FE} = \boldsymbol{\mathcal{P}}^T$.

Now that both operators are defined, the coarse scale system in equation is written algebraically as

$$\boldsymbol{\mathcal{R}}\boldsymbol{A}^{\nu}\boldsymbol{\mathcal{P}}\check{\boldsymbol{x}}_c^{\nu+1/2} = \boldsymbol{\mathcal{R}}\boldsymbol{f}^{\nu}, \tag{4.20}$$

where $\check{\boldsymbol{x}}_c^{\nu+1/2}$ is the coarse scale solution (i.e. pressure or temperature), and the superscript $\nu + 1/2$, indicating that this stage will be complemented by a second stage smoother to be explained later.

Note that in equation 4.20, $(\boldsymbol{\mathcal{R}}\boldsymbol{A}^{\nu}\boldsymbol{\mathcal{P}})$ constructs the coarse system matrix $\boldsymbol{A}_c^{\nu}$. The approximate fine scale solution is found as

$$\boldsymbol{x}'^{\nu+1/2} = \boldsymbol{\mathcal{P}}\check{\boldsymbol{x}}_c^{\nu+1/2} = \boldsymbol{\mathcal{P}}(\boldsymbol{\mathcal{R}}\boldsymbol{A}^{\nu}\boldsymbol{\mathcal{P}})^{-1}\boldsymbol{\mathcal{R}}\boldsymbol{f}^{\nu}, \tag{4.21}$$

or in residual form,

$$\boldsymbol{\delta x}'^{\nu+1/2} = \boldsymbol{\mathcal{P}}\boldsymbol{\delta}\check{\boldsymbol{x}}_c^{\nu+1/2} = \boldsymbol{\mathcal{P}}(\boldsymbol{\mathcal{R}}\boldsymbol{A}^{\nu}\boldsymbol{\mathcal{P}})^{-1}\boldsymbol{\mathcal{R}}\boldsymbol{r}^{\nu}, \tag{4.22}$$

where $\boldsymbol{r}^{\nu}$ is the fine-scale residual and is calculated as $\boldsymbol{r}^{\nu} = \boldsymbol{f}^{\nu} - \boldsymbol{A}^{\nu}\boldsymbol{x}'^{\nu}$.

4.5. Algorithm

In each solver, both $\boldsymbol{\delta p}'^{\nu+1/2}$ and $\boldsymbol{\delta T}'^{\nu+1/2}$ are calculated first using multiscale operators (see equation 4.22), and then a 2^{nd} stage smoother (in this study, ILU(0)) is employed. Here, we employ 5 ILU(0) iterations per stage. This 2-stage multiscale procedure is repeated iteratively until the norm of residual goes below the prescribed tolerance.

ILU(0) is an incomplete factorisation of a sparse matrix (in this case $\boldsymbol{A}^{\nu}$) into a lower triangular matrix $\boldsymbol{L}$ and upper triangular matrix $\boldsymbol{U}$ so that $\boldsymbol{A}^{\nu} \approx \boldsymbol{LU}$ [31]. Therefore, the second stage can be expressed as

$$\boldsymbol{\delta x}'^{\nu+2/2} = \boldsymbol{U}^{-1}(\boldsymbol{L}^{-1}\boldsymbol{r}^{\nu}), \tag{4.23}$$

with the superscript $\nu + 2/2$ indicating the second stage index. The approximate fine scale solution is finally calculated as $\boldsymbol{x}'^{\nu+1} = \boldsymbol{x}'^{\nu} + \boldsymbol{\delta x}'^{\nu+1/2} + \boldsymbol{\delta x}'^{\nu+2/2}$, where $\boldsymbol{x}' \in \{\boldsymbol{p}', \boldsymbol{T}'\}$. The MS algorithms for pressure and temperature are presented in figure 4.5 and 4.6, respectively.

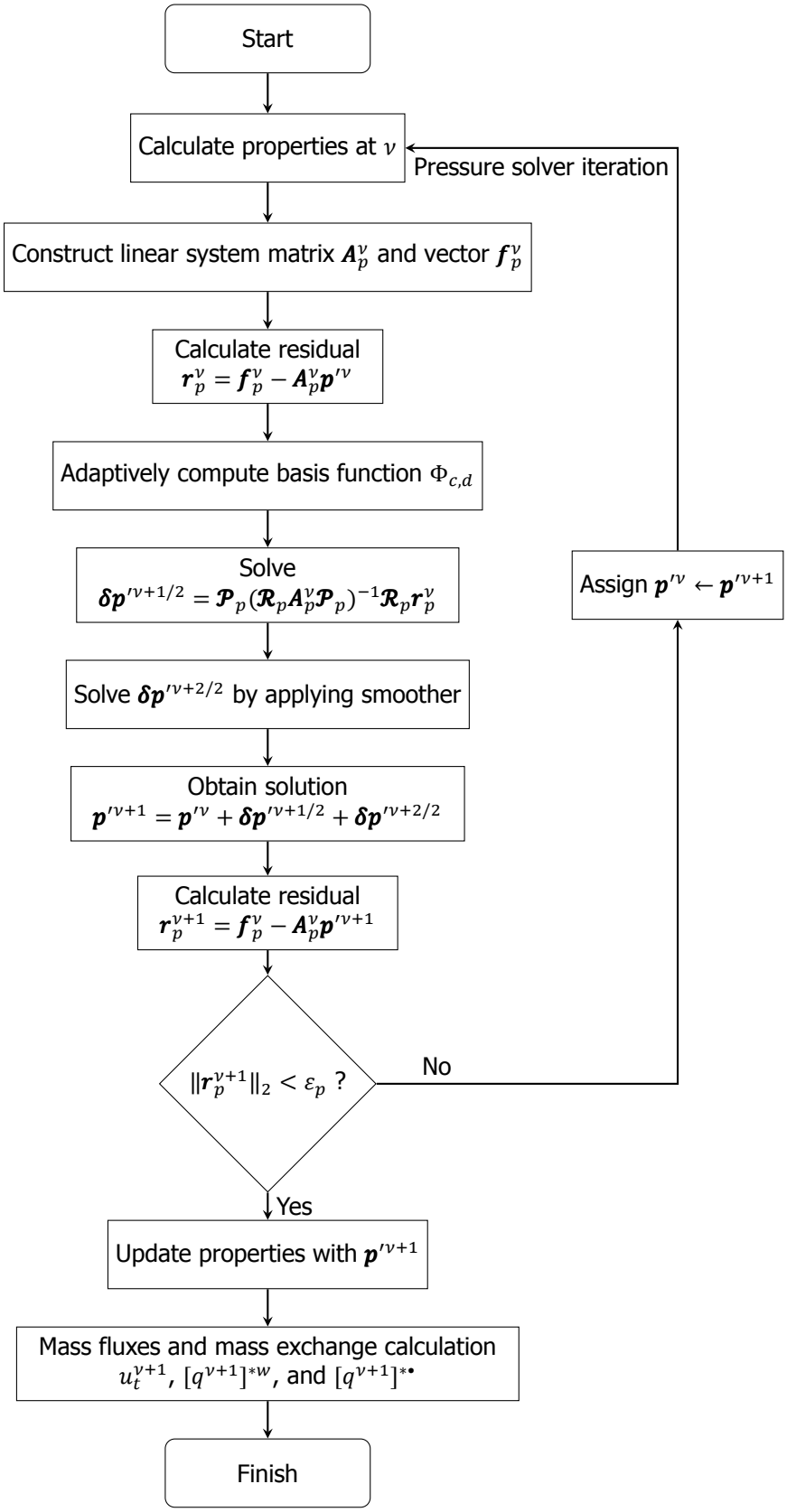

Figure 4.5: Flowchart of MS pressure solver.

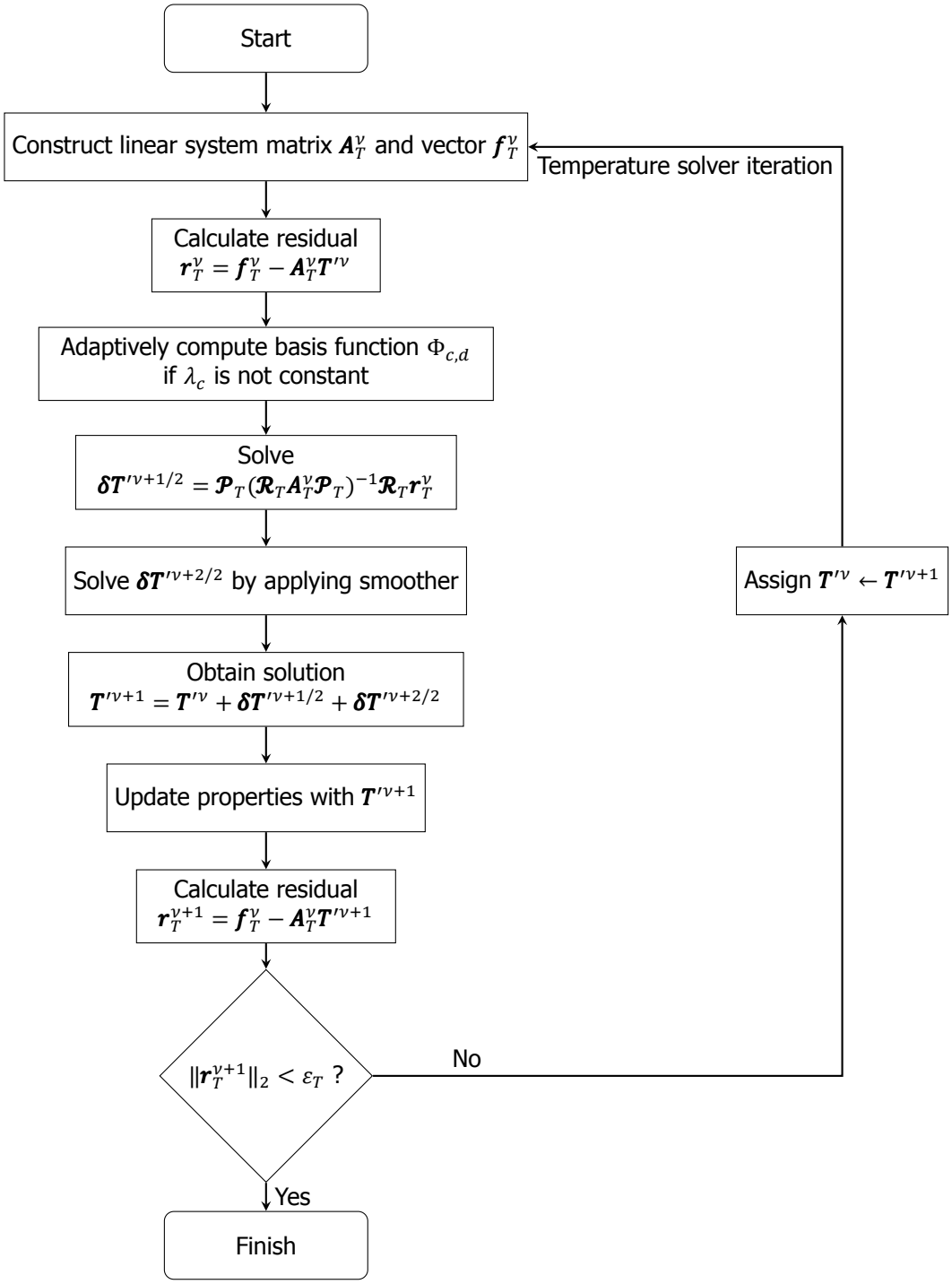

Figure 4.6: Flowchart of MS temperature solver.

5

Results and Discussions

In this chapter, numerical results are presented first to validate the EDFM model for coupled flow-heat equations, and then to investigate the performance of the multiscale simulation strategy for fractured reservoirs.

5.1. Test Case 1: Validation of EDFM Formulation

In this test case, the fine scale EDFM model is validated by comparing it to the result of the fully-resolved Direct Numerical Simulation (DNS). The DNS result is obtained by using a very fine grid such that the fractures are captured as equi-dimensional (heterogeneous) objects [2]. The EDFM, on the other hand, imposes much coarser grids and models the impact of the explicit lower-dimensional fractures by introducing fracture-matrix connectivities.

As shown in figure 5.1, a '+'-shaped fracture network is embedded in the middle of a homogeneous reservoir. The fracture aperture is $0.0101\ m$, which can be fully resolved by imposing 99×99 DNS grid cells. This aperture leads to the fracture permeability of $k^f = 8.50 \times 10^{-6}\ m^2$. The simulation parameters are shown in table 5.1.

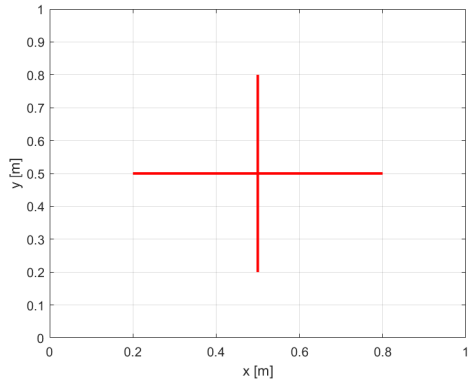

Figure 5.1: Geometry of the '+'-shaped fracture networks crossing the reservoir for test case 1.

Table 5.1: Simulation parameters for test case 1.

Parameters	Values	Parameters	Values
$L_x\ [m]$	1	$p_L\ [Pa]$	2×10^7
$L_y\ [m]$	1	$p_R\ [Pa]$	1×10^7
$\Delta x\ [m]$	0.0101	$C_{pr}\ [J/kg-K]$	920
$\Delta y\ [m]$	0.0101	$\rho_r\ [kg/m^3]$	2650
$t\ [s]$	20000	$\lambda_{cr}\ [W/m-K]$	1.5
$\Delta t\ [s]$	200	$T_i\ [K]$	500
$\phi\ [-]$	0.1	$T_L\ [K]$	300
$k\ [m^2]$	10^{-15}	$\varepsilon_s\ [-]$	10^{-2}
$p_i\ [Pa]$	1×10^7		

Figures 5.2 and 5.3 present the pressure and temperature solutions obtained from EDFM and DNS simulators. Note that the EDFM solutions are obtained by imposing only 11×11 matrix cells and 14 fracture elements. It is clear that the EDFM solutions are in good agreement with the DNS reference ones.

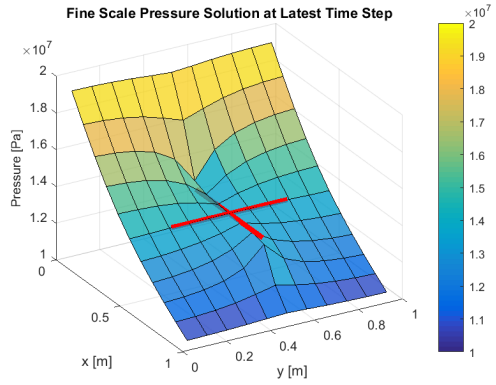

(a) EDFM pressure solution (surface plot).

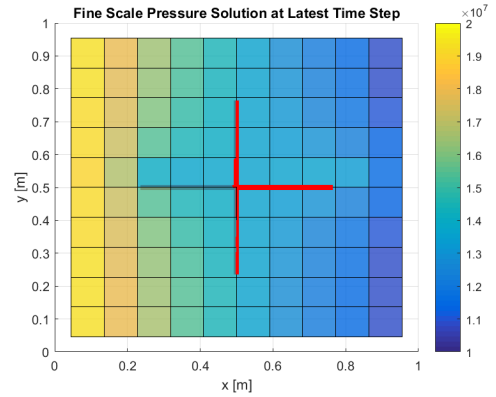

(b) EDFM pressure solution (top view).

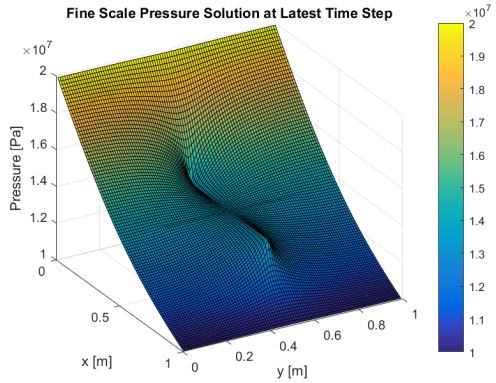

(c) DNS pressure solution (surface plot).

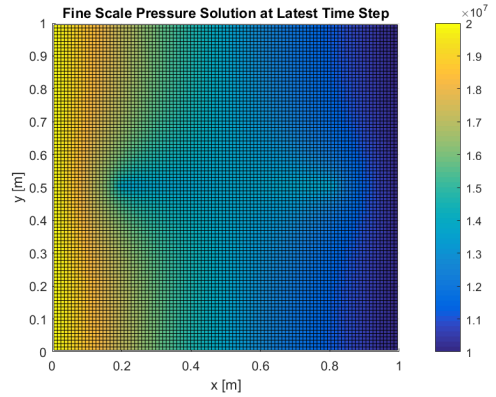

(d) DNS pressure solution (top view).

Figure 5.2: EDFM pressure surface plot (a) and top view (b), and DNS pressure surface plot (c) and top view (d) at $t = 20000s$ for a reservoir model with the dimension of $1\ m \times 1\ m$. The EDFM model is resolved with the resolution of 11×11 matrix cells and 14 fracture elements, while the DNS model is resolved with the resolution of 99×99 matrix cells.

The error norms for pressure and temperature values are calculated based on

$$\|e_x\|_2 = \frac{\|\boldsymbol{x_{EDFM}} - \boldsymbol{x_{DNS}}\|_2}{\|\boldsymbol{x_{DNS}}\|_2}, \tag{5.1}$$

assuming $\|\boldsymbol{x_{DNS}}\|_2 \neq 0$, where $\boldsymbol{x}$ is flow rate $\boldsymbol{q}$ for pressure and enthalpy flux $\boldsymbol{q}_H$ for temperature at both left and right boundary faces. The error norms for both pressure and temperature at different time

steps are plotted, normalised with the Pore Volume Injected (PVI), and shown in figure 5.4. This figure also presents the EDFM error study at different times for the case when 33×33 EDFM grids are imposed, with 40 fracture elements. More specifically, the error is due to: (1) significant difference between the grid resolutions imposed by each method and (2) the error of EDFM fracture model. Nevertheless, the two approach are in good agreement. Note that a more consistent extension of EDFM is being recently introduced as Projection-based EDFM (pEDFM), where the grid convergence study for both EDFM and pEDFM is also studied [32].

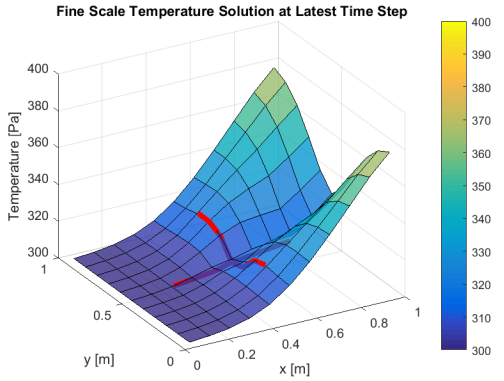

(a) EDFM temperature solution (surface plot).

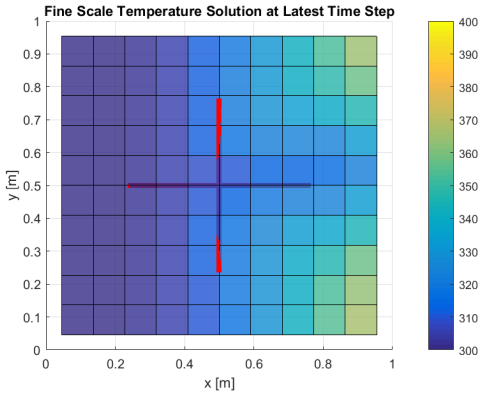

(b) EDFM temperature solution (top view).

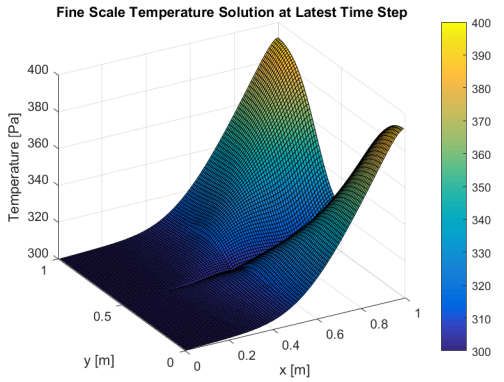

(c) DNS temperature solution (surface plot).

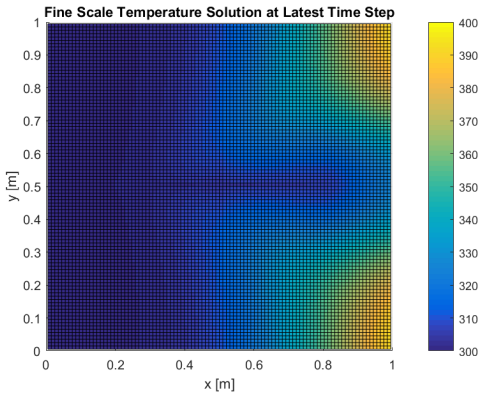

(d) DNS temperature solution (top view).

Figure 5.3: EDFM temperature surface plot (a) and top view (b), and DNS temperature surface plot (c) and top view (d) at $t = 20000s$ for reservoir model with the dimension of $1\ m \times 1\ m$. The EDFM model is resolved with the resolution of 11×11 matrix cells and 14 fracture elements, while the DNS model is resolved with the resolution of 99×99 matrix cells.

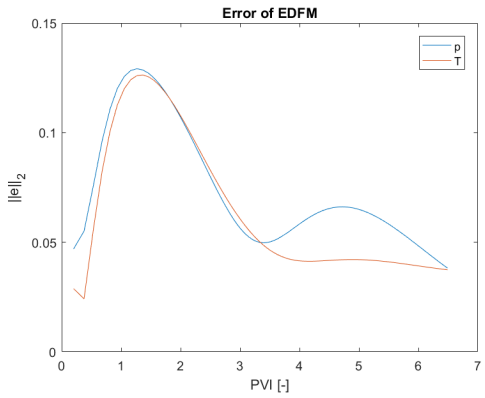

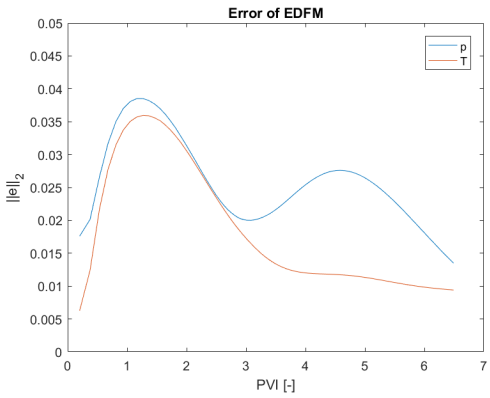

Figure 5.4: Error norm of EDFM pressure and temperature solution at different times with different grid resolutions: 11×11 (left) and 33×33 (right).

5.2. Test Case 2: Homogeneous Reservoir with a Diagonal Fracture

A quarter of a five spot test case is considered in a homogeneous reservoir with a diagonal fracture. The simulation parameters are shown in table 5.2. EDFM imposes 85 fracture and 99×99 matrix elements. The geometry of the fracture within the reservoir is shown in figure 5.5. The multiscale simulator imposes 9×9 coarse grids for matrix and 8 for fractures with two different coupling strategies for basis function calculation.

Table 5.2: Simulation parameters for test case 2.

Parameters	Values	Parameters	Values
$L_x\ [m]$	99	$p_{inj}\ [Pa]$	2×10^7
$L_y\ [m]$	99	$p_{prod}\ [Pa]$	1×10^7
$\Delta x\ [m]$	1	$C_{pr}\ [J/kg-K]$	840
$\Delta y\ [m]$	1	$\rho_r\ [kg/m^3]$	2700
$Coarsening\ ratio\ [-]$	11	$\lambda_{cr}\ [W/m-K]$	2.9
$t\ [years]$	1	$T_i\ [K]$	500
$\phi\ [-]$	0.15	$T_{inj}\ [K]$	300
$k\ [m^2]$	10^{-14}	$\varepsilon_s\ [-]$	10^{-2}
$PI\ [m]$	10	$\varepsilon_p\ [-]$	10^{-6}
$p_i\ [Pa]$	1×10^7	$\varepsilon_T\ [-]$	10^{-1}

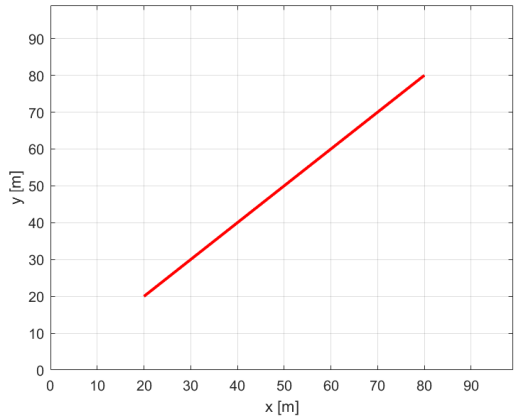

Figure 5.5: Geometry of a single diagonal fracture crossing the reservoir for test case 2.

Figures 5.6 and 5.7 show the converged solution of both fine scale reference as well as multiscale pressure and temperature. The white lines shown in the plots are the primal coarse cell boundaries. The relative error norms of the multiscale solution obtained are $\|e_p\|_2 = 2.65 \times 10^{-5}$ and $\|e_T\|_2 = 1.62 \times 10^{-5}$ (Decoupled-AMS), and $\|e_p\|_2 = 2.18 \times 10^{-5}$ and $\|e_T\|_2 = 1.58 \times 10^{-5}$ (Frac-AMS). It is shown that both Decoupled-AMS and Frac-AMS result in very good approximations and therefore, very low errors.

The multiscale pressure and temperature solutions at the first iteration (before smoothing) are also presented in figure 5.8 and 5.9, respectively, to show that the multiscale provides very good approximations even with no 2nd stage smoother nor any other (inner and outer) iteration employed. These results are also compared to the reference fine scale solutions, demonstrating the accuracy of the developed multiscale formulation.

Decoupled-AMS for pressure calculation results in slightly higher error at the fracture tips, where – as expected – the interaction of matrix and fracture domain is relatively high. Note that the temperature field experiences a rapid change in the location of the fracture, due to rapid transport of cold water through the fractures. As such, the significant temperature contrast is created fairly quickly throughout the reservoir, leading to strong nonlinear time-dependent solution field. This is clear from results

presented in figure 5.7. Nevertheless, as shown, the multiscale method can represent the complex solution field accurately, even with no smoothing stage.

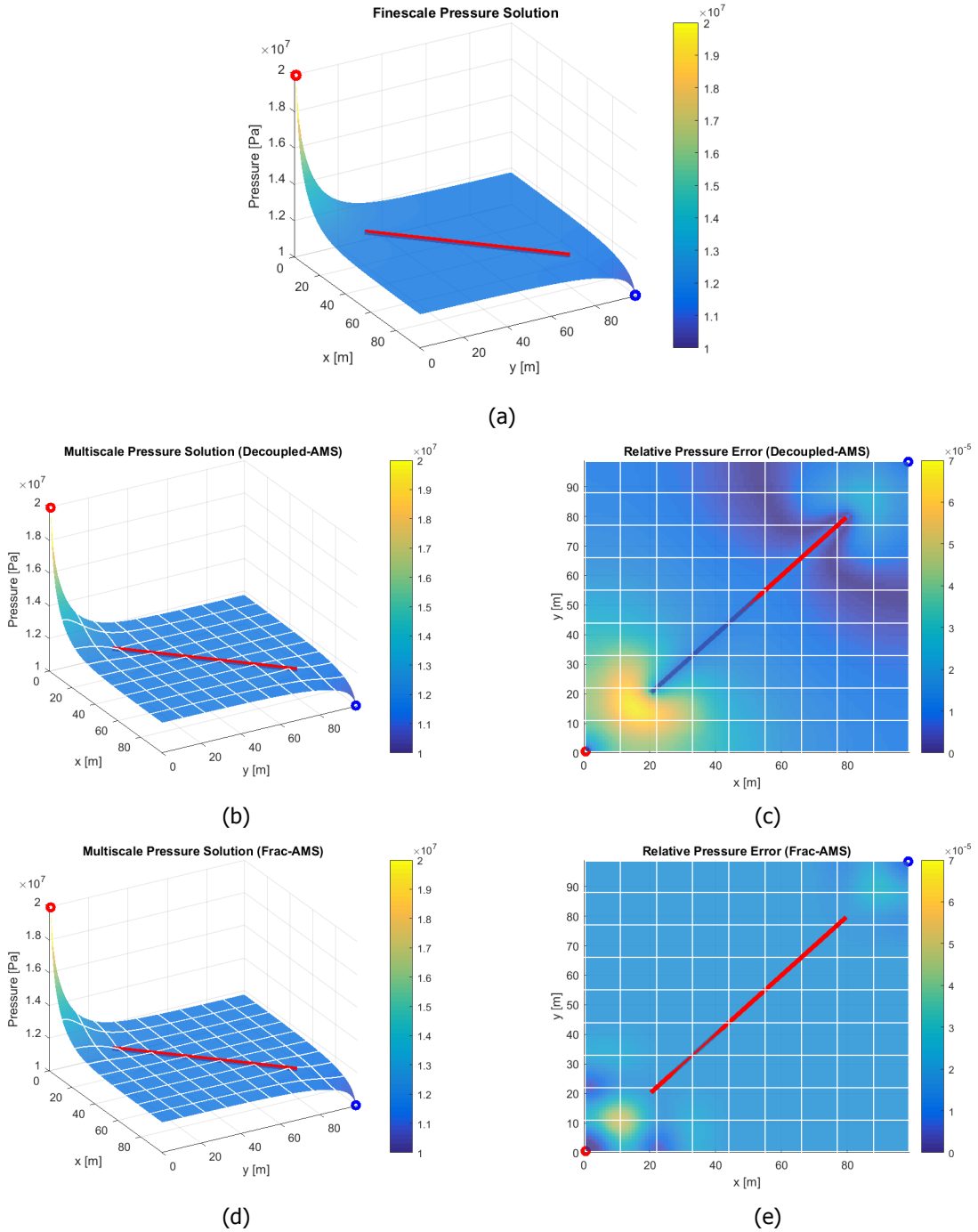

Figure 5.6: Fine-scale reference pressure with 99×99 matrix and 85 fracture elements (a) and multiscale approximate pressure solutions obtained using Decoupled-AMS (b) and Frac-AMS (d) methods with 9×9 coarse matrix and 8 fracture grid cells at convergence. The corresponding relative error norms (c and e) are $\|e_p\|_2 = 2.65 \times 10^{-5}$ (Decoupled-AMS) and $\|e_p\|_2 = 2.18 \times 10^{-5}$ (Frac-AMS).

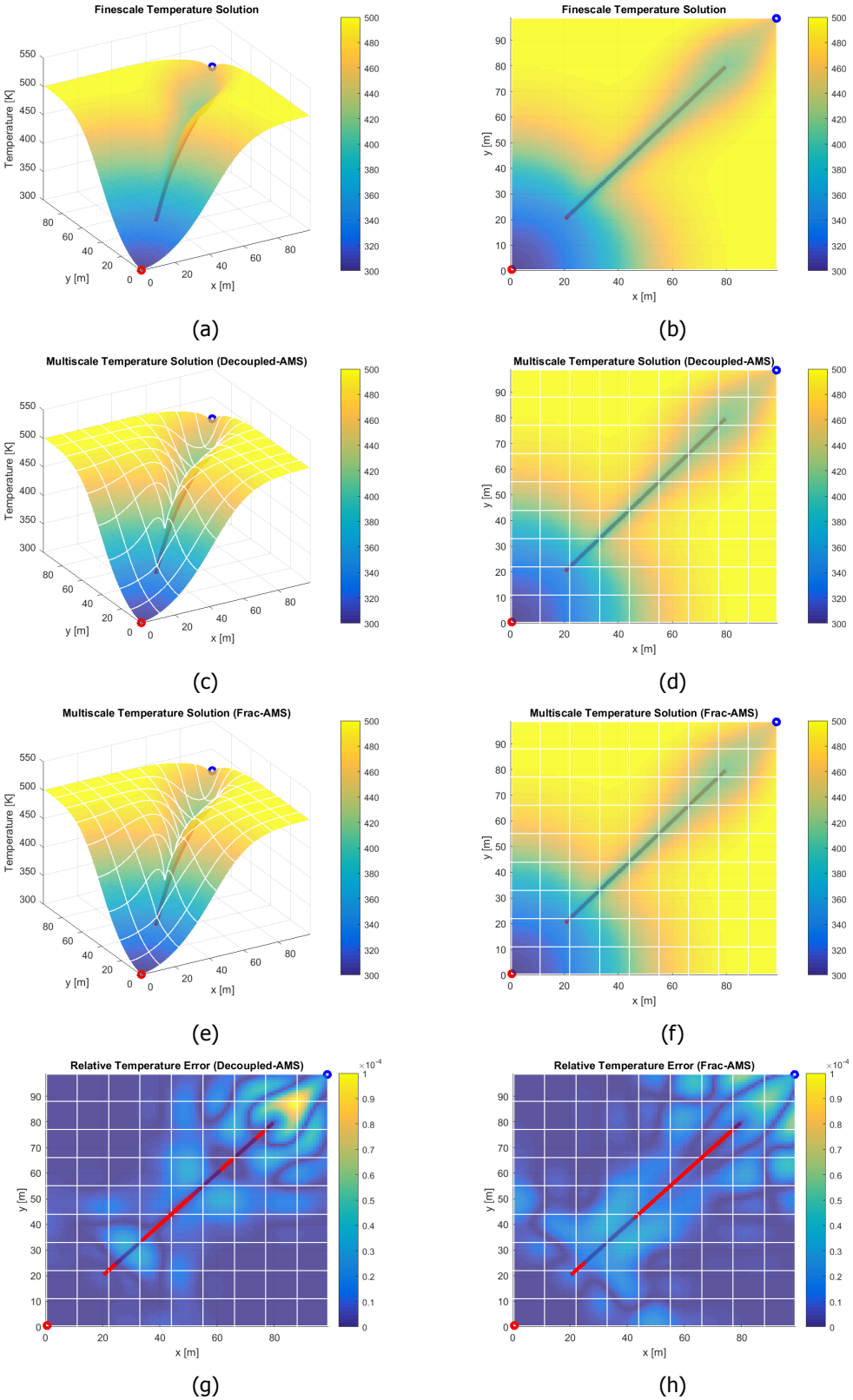

Figure 5.7: Fine-scale (a and b) reference temperature obtained with 99×99 grid cells and 85 fracture elements, and multiscale approximate temperature solutions obtained using Decoupled-AMS (c and d) and Frac-AMS (e and f) methods in surface plot (left column) and top view (right column) with 9×9 coarse matrix and 8 fracture grid cells at convergence. The corresponding relative error norms (g and h) are $\|e_T\|_2 = 1.62 \times 10^{-5}$ (Decoupled-AMS) and $\|e_T\|_2 = 1.58 \times 10^{-5}$ (Frac-AMS).

At the first iteration stage, the relative error norms of the multiscale solution obtained before smoothing are $\|e_p\|_2 = 0.0081$ and $\|e_T\|_2 = 0.0343$ (Decoupled-AMS), and $\|e_p\|_2 = 0.0016$ and $\|e_T\|_2 = 0.0198$ (Frac-AMS). After 1 stage of smoothing, the errors are reduced to $\|e_p\|_2 = 0.0076$ and $\|e_T\|_2 = 0.0146$ (Decoupled-AMS) and $\|e_p\|_2 = 0.0008$ and $\|e_T\|_2 = 0.0035$ (Frac-AMS).

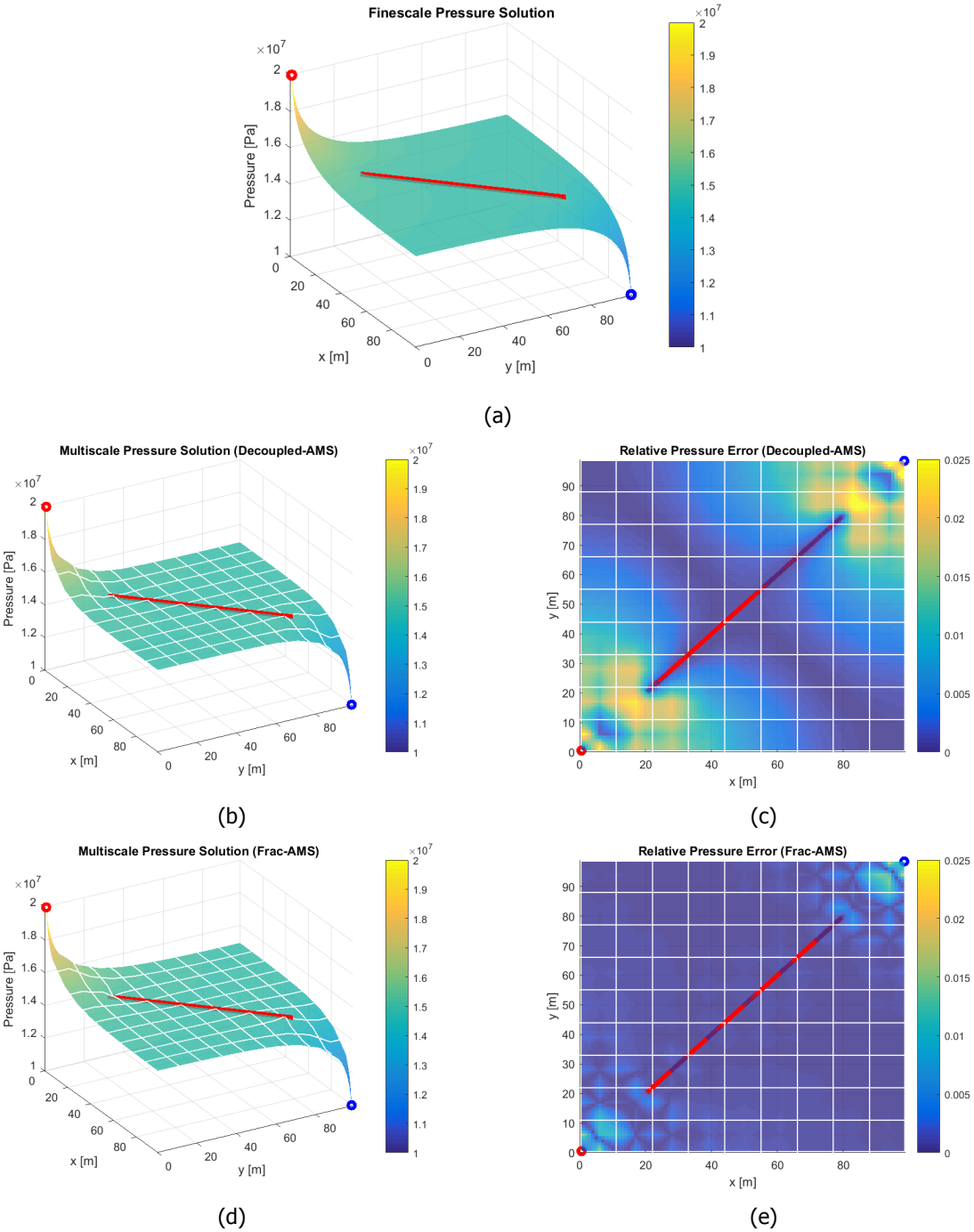

Figure 5.8: Fine-scale reference pressure with 99×99 matrix and 85 fracture elements (a) and multiscale approximate pressure solutions obtained using Decoupled-AMS (b) and Frac-AMS (d) methods with 9×9 coarse matrix and 8 fracture grid cells at the first iteration stage before smoothing. The corresponding relative error norms (c and e) are $\|e_p\|_2 = 0.0081$ (Decoupled-AMS) and $\|e_p\|_2 = 0.0016$ (Frac-AMS). After 1 stage of smoothing these errors reduce to $\|e_p\|_2 = 0.0076$ (Decoupled-AMS) and $\|e_p\|_2 = 0.0008$ (Frac-AMS).

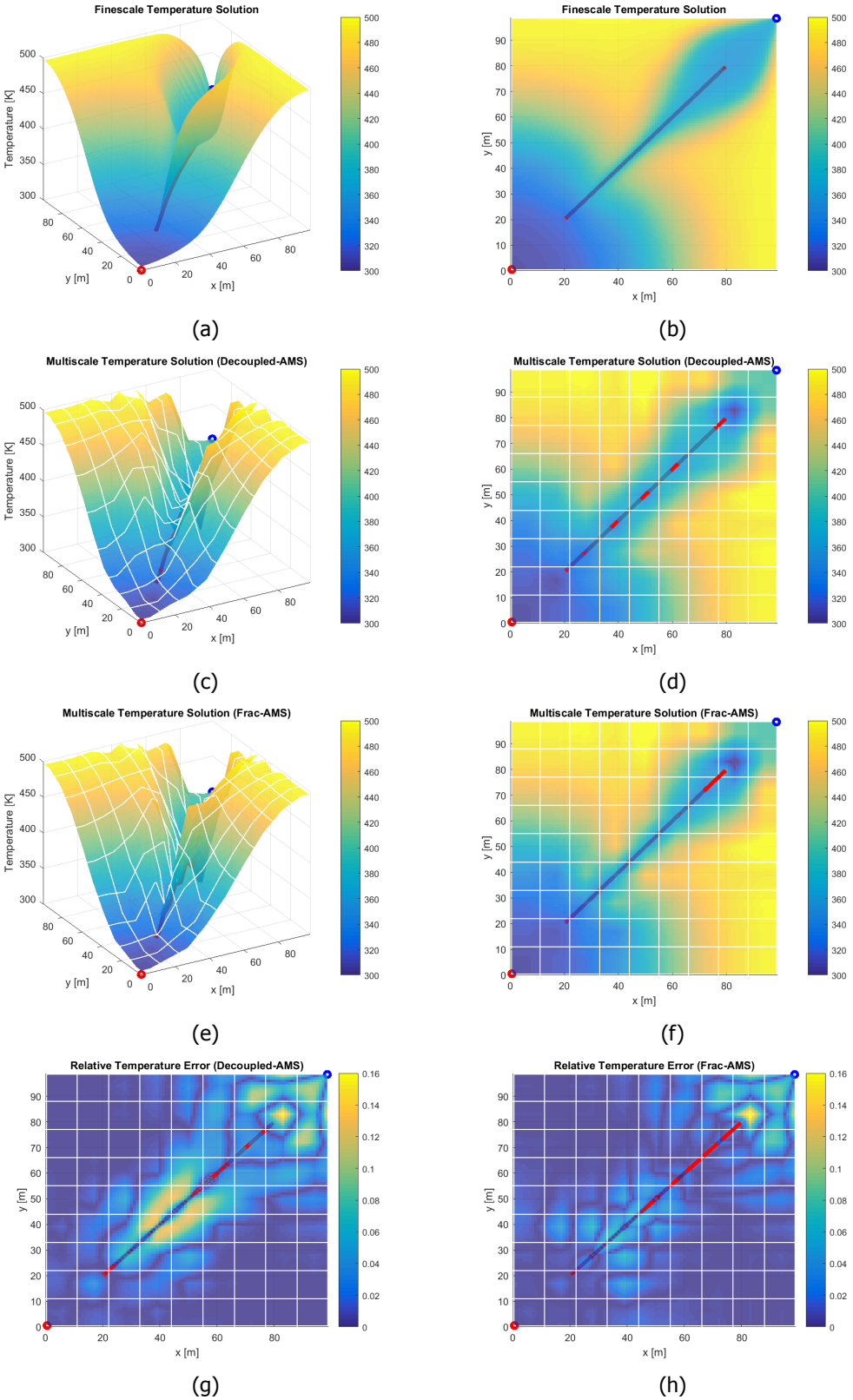

Figure 5.9: Fine-scale (a and b) reference temperature obtained with 99×99 grid cells and 85 fracture elements, and multiscale approximate temperature solutions obtained using Decoupled-AMS (c and d) and Frac-AMS (e and f) methods in surface plot (left column) and top view (right column) with 9×9 coarse matrix and 8 fracture grid cells at the first iteration stage before smoothing. The corresponding relative error norms (g and h) are $\|e_T\|_2 = 0.0343$ (Decoupled-AMS) and $\|e_T\|_2 = 0.0198$ (Frac-AMS). After 1 stage of smoothing these errors reduce to $\|e_T\|_2 = 0.0146$ (Decoupled-AMS) and $\|e_T\|_2 = 0.0035$ (Frac-AMS).

The partially coupled approach (Frac-AMS) leads to lower errors compared to Decoupled-AMS, especially in the area surrounding the fracture. However, it does not bring much improvements. The errors obtained using Decoupled-AMS are not significant and could be resolved with several smoothing and iterations. A more detailed performance comparison for both method is needed to conclusively determine the most efficient strategy.

5.3. Test Case 3: Heterogeneous Reservoir with Random Fracture Networks

A line drive test case is considered in a heterogeneous reservoir with random fracture networks. The log_{10} of permeability and average thermal conductivity are plotted in figure 5.10, and the simulation parameters are shown in table 5.3. EDFM imposes 391 fracture and 150×150 matrix elements. The geometry of the fractures within the reservoir is shown in figure 5.11. The multiscale simulator imposes 10×10 coarse grids for matrix and 26 for fractures with two different coupling strategies for basis function calculation.

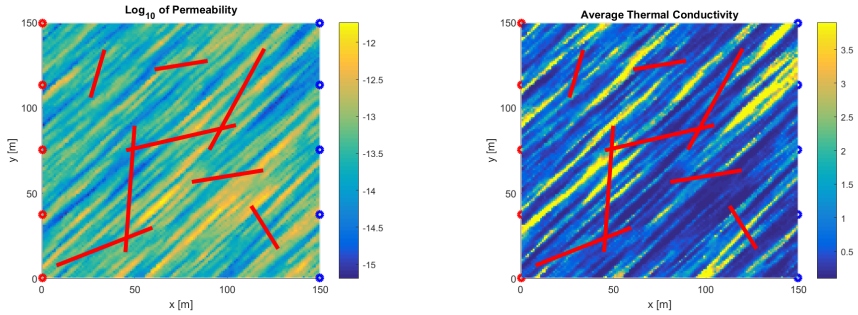

Figure 5.10: Log_{10} of permeability (left) and average thermal conductivity (b) for a reservoir model with the dimension of $150\ m \times 150\ m$, with the fine scale resolution of 150×150 cells for test case 3.

Table 5.3: Simulation parameters for test case 3.

Parameters	Values	Parameters	Values
$L_x\ [m]$	150	$p_{inj}\ [Pa]$	2×10^7
$L_y\ [m]$	150	$p_{prod}\ [Pa]$	1×10^7
$\Delta x\ [m]$	1	$C_{pr}\ [J/kg-K]$	760
$\Delta y\ [m]$	1	$\rho_r\ [kg/m^3]$	2160
$Coarsening\ ratio\ [-]$	15	$T_i\ [K]$	500
$t\ [years]$	0.75	$T_{inj}\ [K]$	300
$\phi\ [-]$	0.1	$\varepsilon_s\ [-]$	10^{-2}
$PI\ [m]$	10	$\varepsilon_p\ [-]$	10^{-6}
$p_i\ [Pa]$	1×10^7	$\varepsilon_T\ [-]$	10^{-1}

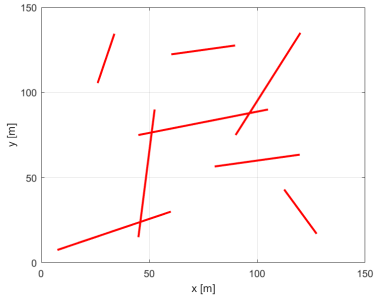

Figure 5.11: Geometry of random fracture networks for test case 3.

Figures 5.12 and 5.13 show the converged solution of both fine scale reference as well as multiscale pressure and temperature. The relative error norms of the multiscale solution obtained are $\|e_p\|_2 = 9.27\times10^{-6}$ and $\|e_T\|_2 = 2.10\times10^{-5}$ (Decoupled-AMS), and $\|e_p\|_2 = 8.08\times10^{-6}$ and $\|e_T\|_2 = 1.59\times10^{-5}$ (Frac-AMS).

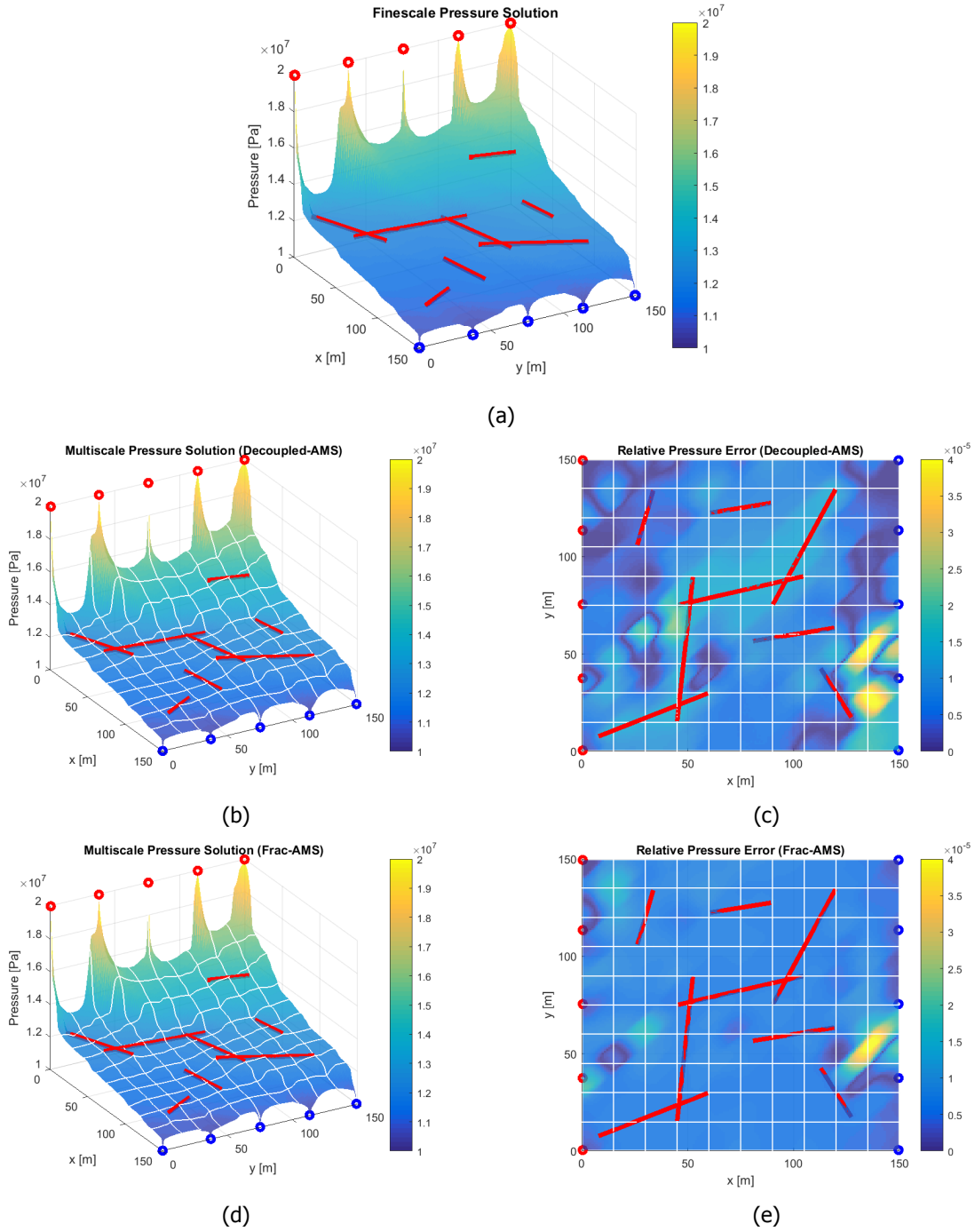

Figure 5.12: Fine-scale reference pressure with 150×150 matrix and 391 fracture elements (a) and multiscale approximate pressure solutions obtained using Decoupled-AMS (b) and Frac-AMS (d) methods with 10×10 coarse matrix and 26 fracture grid cells at convergence. The corresponding relative error norms (c and e) are $\|e_p\|_2 = 9.27 \times 10^{-6}$ (Decoupled-AMS) and $\|e_p\|_2 = 8.08 \times 10^{-6}$ (Frac-AMS).

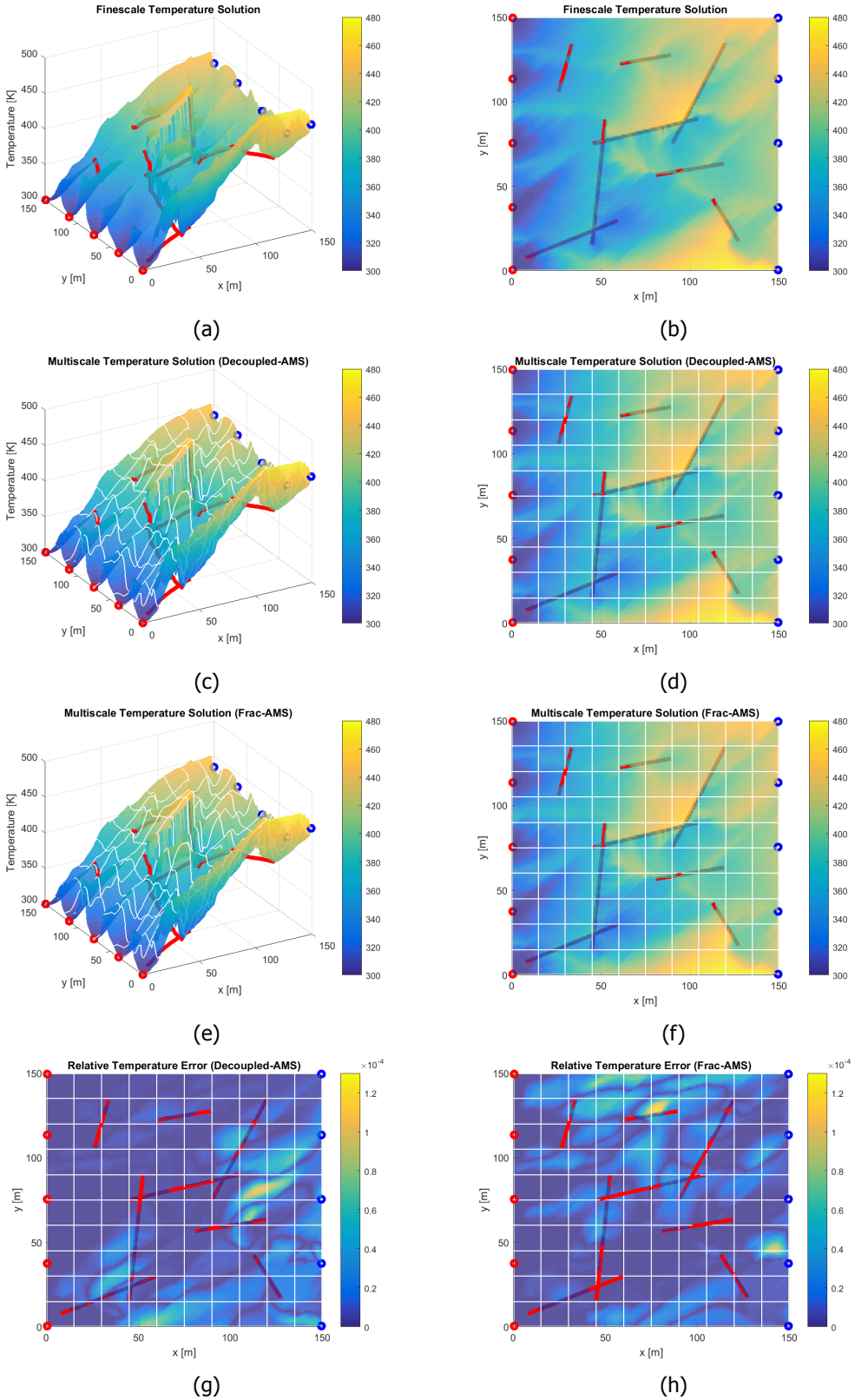

Figure 5.13: Fine-scale (a and b) reference temperature obtained with 150×150 grid cells and 391 fracture elements, and multiscale approximate temperature solutions obtained using Decoupled-AMS (c and d) and Frac-AMS (e and f) methods in surface plot (left column) and top view (right column) with 10×10 coarse matrix and 26 fracture grid cells at convergence. The corresponding relative error norms (g and h) are $\|e_T\|_2 = 2.10 \times 10^{-5}$ (Decoupled-AMS) and $\|e_T\|_2 = 1.59 \times 10^{-5}$ (Frac-AMS).

Again, the multiscale pressure and temperature solutions at the first iteration (before smoothing) are also presented in figure 5.14 and 5.15, respectively. The multiscale solutions obtained using Decoupled-AMS and Frac-AMS do not differ significantly. The first solution before smoothing is shown to approximate the shape of the fine scale solution really well, even though there are still some errors. For Decoupled-AMS, these errors are slightly higher especially near the fractures.

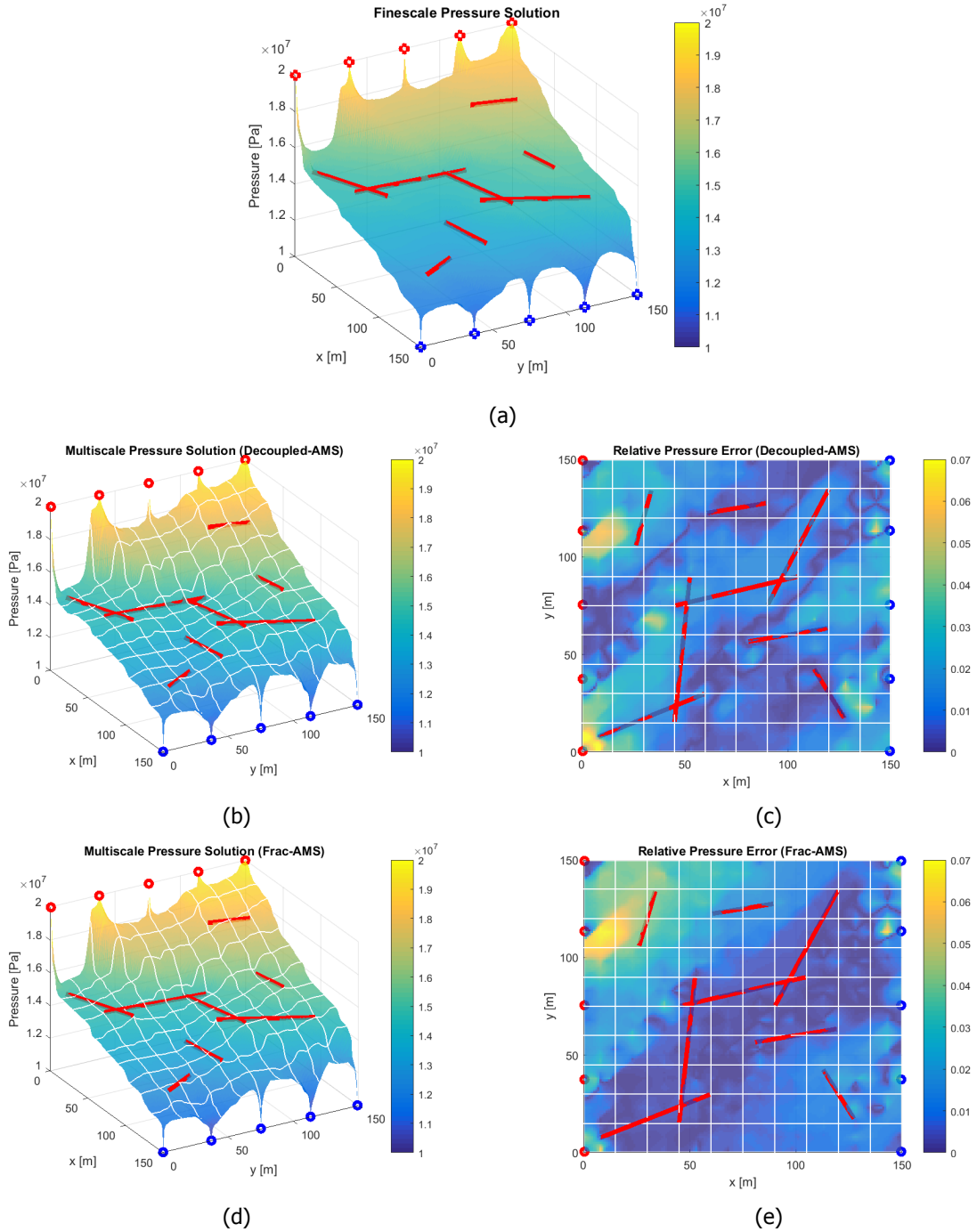

Figure 5.14: Fine-scale reference pressure with 150×150 matrix and 391 fracture elements (a) and multiscale approximate pressure solutions obtained using Decoupled-AMS (b) and Frac-AMS (d) methods with 10×10 coarse matrix and 26 fracture grid cells at the first iteration stage before smoothing. The corresponding relative error norms (c and e) are $\|e_p\|_2 = 0.0181$ (Decoupled-AMS) and $\|e_p\|_2 = 0.0206$ (Frac-AMS). After 1 stage of smoothing these errors reduce to $\|e_p\|_2 = 0.0172$ (Decoupled-AMS) and $\|e_p\|_2 = 0.0204$ (Frac-AMS)

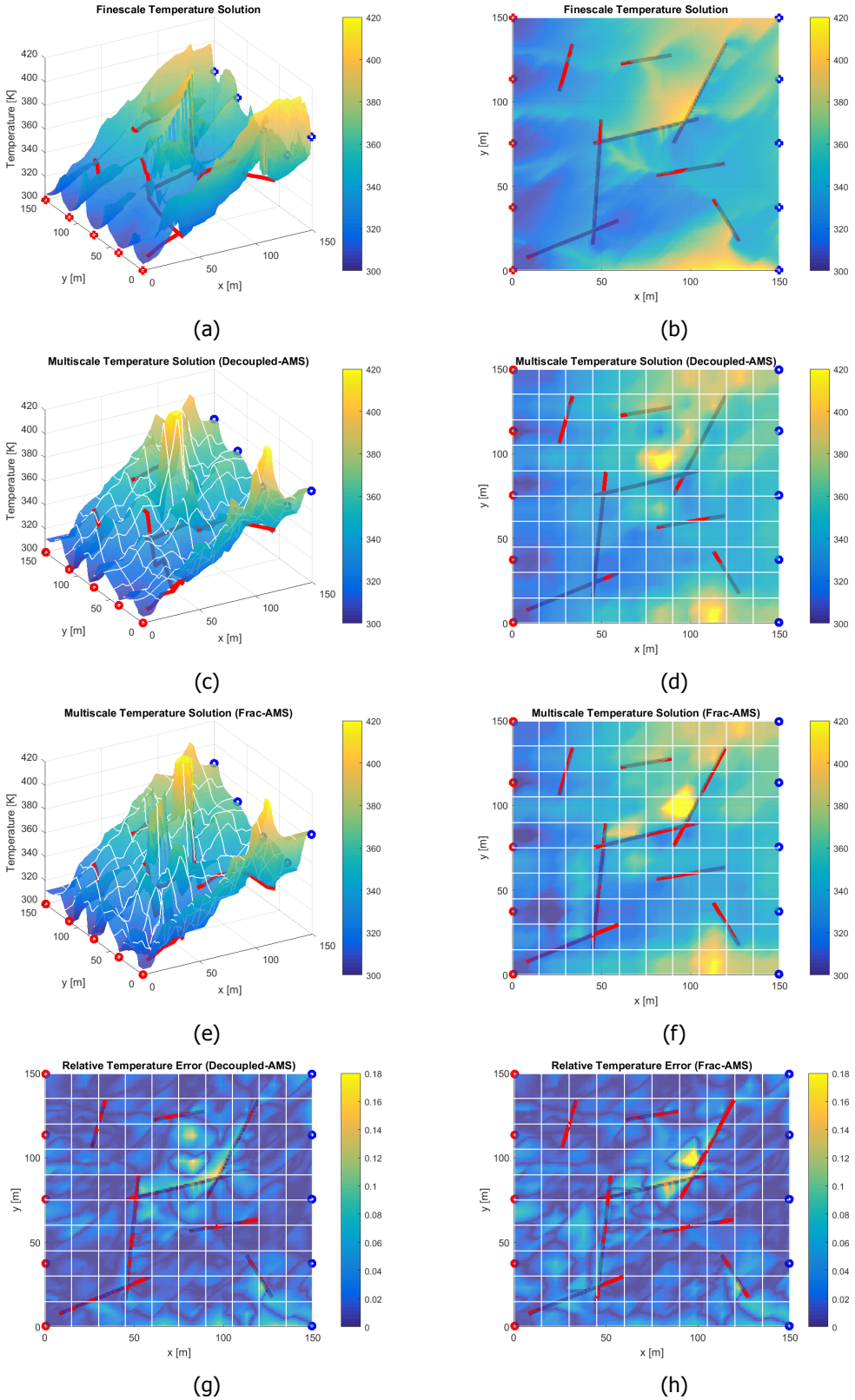

Figure 5.15: Fine-scale (a and b) reference temperature obtained with 150×150 grid cells and 391 fracture elements, and multiscale approximate temperature solutions obtained using Decoupled-AMS (c and d) and Frac-AMS (e and f) methods in surface plot (left column) and top view (right column) with 10×10 coarse matrix and 26 fracture grid cells at the first iteration stage before smoothing. The corresponding relative error norms (g and h) are $\|e_T\|_2 = 0.0285$ (Decoupled-AMS) and $\|e_T\|_2 = 0.0308$ (Frac-AMS). After 1 stage of smoothing these errors reduce to $\|e_T\|_2 = 0.0081$ (Decoupled-AMS) and $\|e_T\|_2 = 0.0091$ (Frac-AMS).

The relative error norms of the multiscale solutions before smoothing are $\|e_p\|_2 = 0.0181$ and $\|e_T\|_2 = 0.0285$ (Decoupled-AMS), and $\|e_p\|_2 = 0.0206$ and $\|e_T\|_2 = 0.0308$ (Frac-AMS). After smoothing, the errors reduce to $\|e_p\|_2 = 0.0172$ and $\|e_T\|_2 = 0.0081$ (Decoupled-AMS) and $\|e_p\|_2 = 0.0204$ and $\|e_T\|_2 = 0.0091$ (Frac-AMS). Note that, as well as the fracture-matrix coupling and nonlinearity of the solution space, the heterogeneity of the reservoir is also one of the factors affecting the errors. Nevertheless, this test case also shows that the multiscale method is highly capable to provide accurate solutions even in presence of highly heterogeneous permeability fields.

5.4. Test Case 4: Heterogeneous Reservoir with Dense Fracture Networks from Outcrop Data

A quarter of a five spot test case is considered in a heterogeneous reservoir with dense and complex fracture networks taken (by applied geologists of TU Delft) from outcrop data in Brazil [3]. The log_{10} of permeability and average thermal conductivity are plotted in figure 5.16, and the simulation parameters are shown in table 5.4. EDFM generates 3860 fracture and 100×100 matrix elements. The geometry of the fractures within the reservoir is shown in figure 5.17. The multiscale simulator imposes 10×10 coarse grids for matrix and 386 for fractures. For this test case, all the results presented are using Decoupled-AMS method.

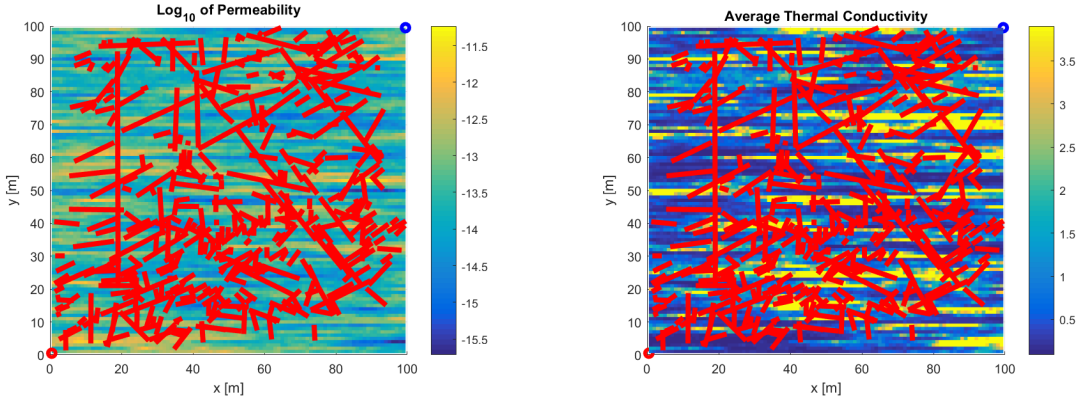

Figure 5.16: Log_{10} of permeability (left) and average thermal conductivity (right) for reservoir model with the dimension of $100\ m \times 100\ m$, with the fine scale resolution of 100×100 cells for test case 4.

Table 5.4: Simulation parameters for test case 4.

Parameters	Values	Parameters	Values
$L_x\ [m]$	100	$p_{inj}\ [Pa]$	2×10^7
$L_y\ [m]$	100	$p_{prod}\ [Pa]$	1×10^7
$\Delta x\ [m]$	1	$C_{pr}\ [J/kg-K]$	827
$\Delta y\ [m]$	1	$\rho_r\ [kg/m^3]$	2600
$Coarsening\ ratio\ [-]$	10	$T_i\ [K]$	500
$t\ [years]$	0.25	$T_{inj}\ [K]$	300
$\phi\ [-]$	0.1	$\varepsilon_s\ [-]$	10^{-2}
$PI\ [m]$	10	$\varepsilon_p\ [-]$	10^{-6}
$p_i\ [Pa]$	1×10^7	$\varepsilon_T\ [-]$	10^{-1}

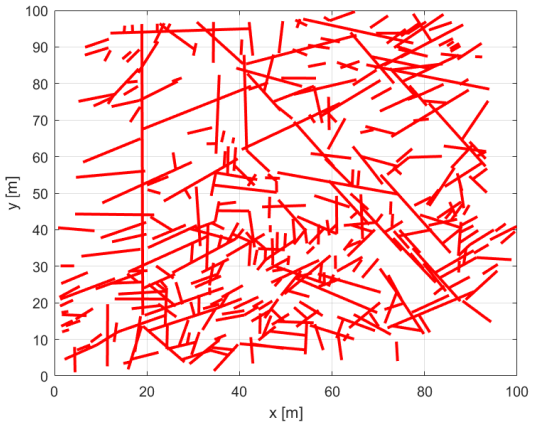

Figure 5.17: Fracture geometry taken from outcrop data [3].

Figures 5.18 and 5.19 show the converged solution of both fine scale reference as well as multiscale pressure and temperature. The relative error norms of the multiscale solution obtained are $\|e_p\|_2 = 8.22 \times 10^{-6}$ and $\|e_T\|_2 = 7.07 \times 10^{-6}$.

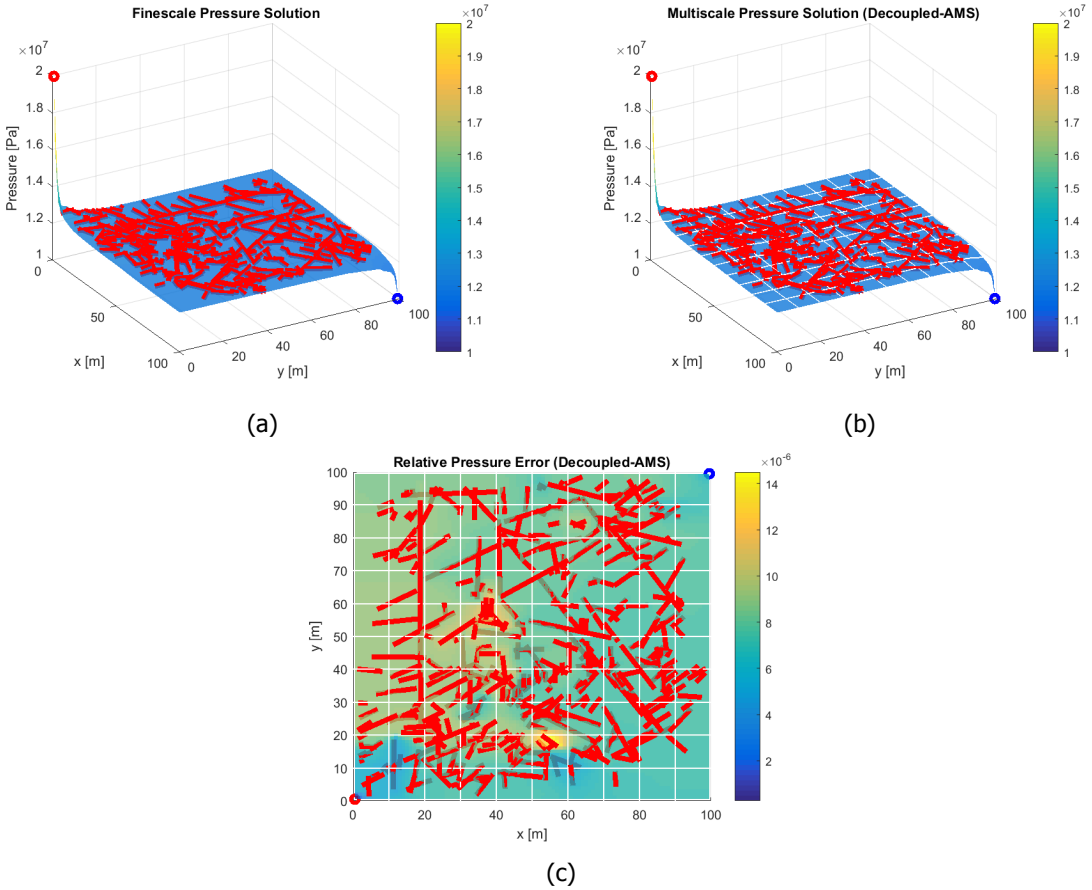

Figure 5.18: Fine-scale reference pressure with 100×100 matrix and 3860 fracture elements (a) and multiscale approximate pressure solution obtained using Decoupled-AMS (b) method with 10×10 coarse matrix and 386 fracture grid cells at convergence. The corresponding relative error norm (c) is $\|e_p\|_2 = 8.22 \times 10^{-6}$.

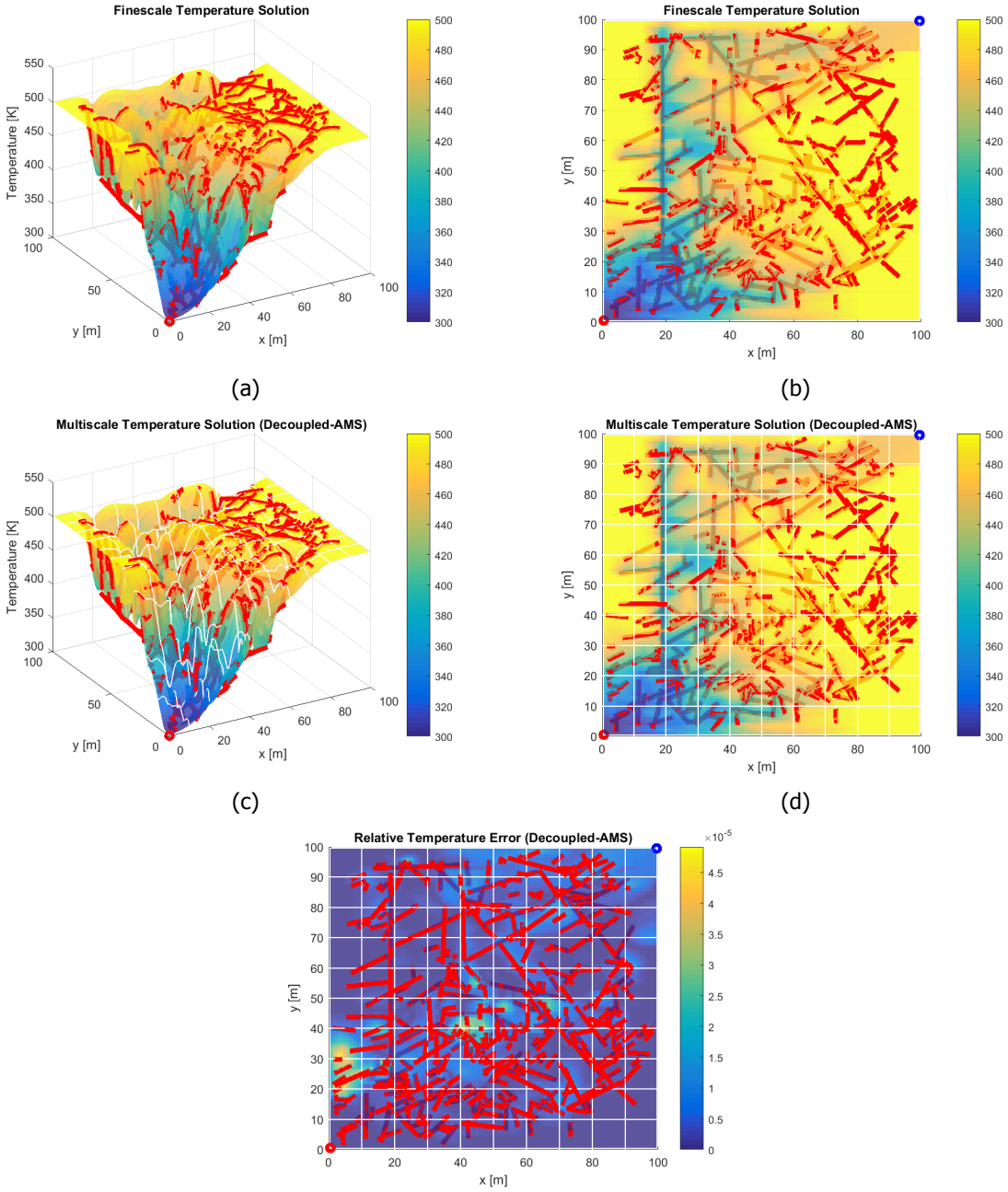

Figure 5.19: Fine-scale (a and b) obtained with 100×100 grid cells and 3860 fracture elements, and multiscale approximate temperature solution obtained using Decoupled-AMS (c and d) method in surface plot (left column) and top view (right column) with 10×10 coarse matrix and 386 fracture grid cells at convergence. The corresponding relative error norm (e) is $\|e_T\|_2 = 7.07 \times 10^{-6}$.

The multiscale solutions for both pressure and temperature at the first iteration stage before smoothing, along with the fine scale reference solutions for comparison, are shown in figure 5.20 and 5.21. The corresponding relative error norms before smoothing are $\|e_p\|_2 = 0.0111$ and $\|e_T\|_2 = 0.0467$, which are relatively low for a complex model. After smoothing, the errors are further reduced to $\|e_p\|_2 = 0.0110$ and $\|e_T\|_2 = 0.0180$.

From the results obtained, it can be concluded that Decoupled-AMS method gives reasonably good approximations, even before the smoothing stage for a heterogeneous system and very dense fracture networks.

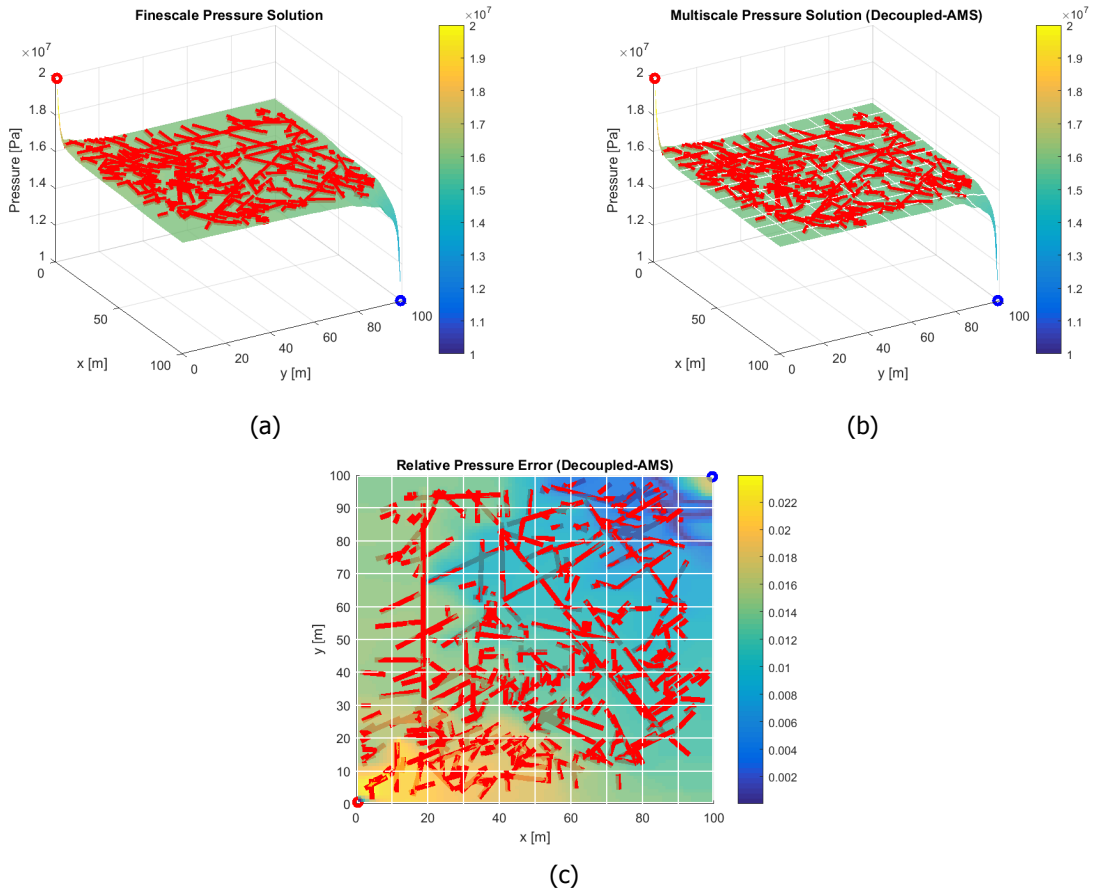

Figure 5.20: Fine-scale reference pressure with 100×100 matrix and 3860 fracture elements (a) and multiscale approximate pressure solution obtained using Decoupled-AMS (b) method with 10×10 coarse matrix and 386 fracture grid cells at the first iteration stage before smoothing. The corresponding relative error norm (c) is $\|e_p\|_2 = 0.0111$. After 1 stage of smoothing this error reduces to $\|e_p\|_2 = 0.0110$.

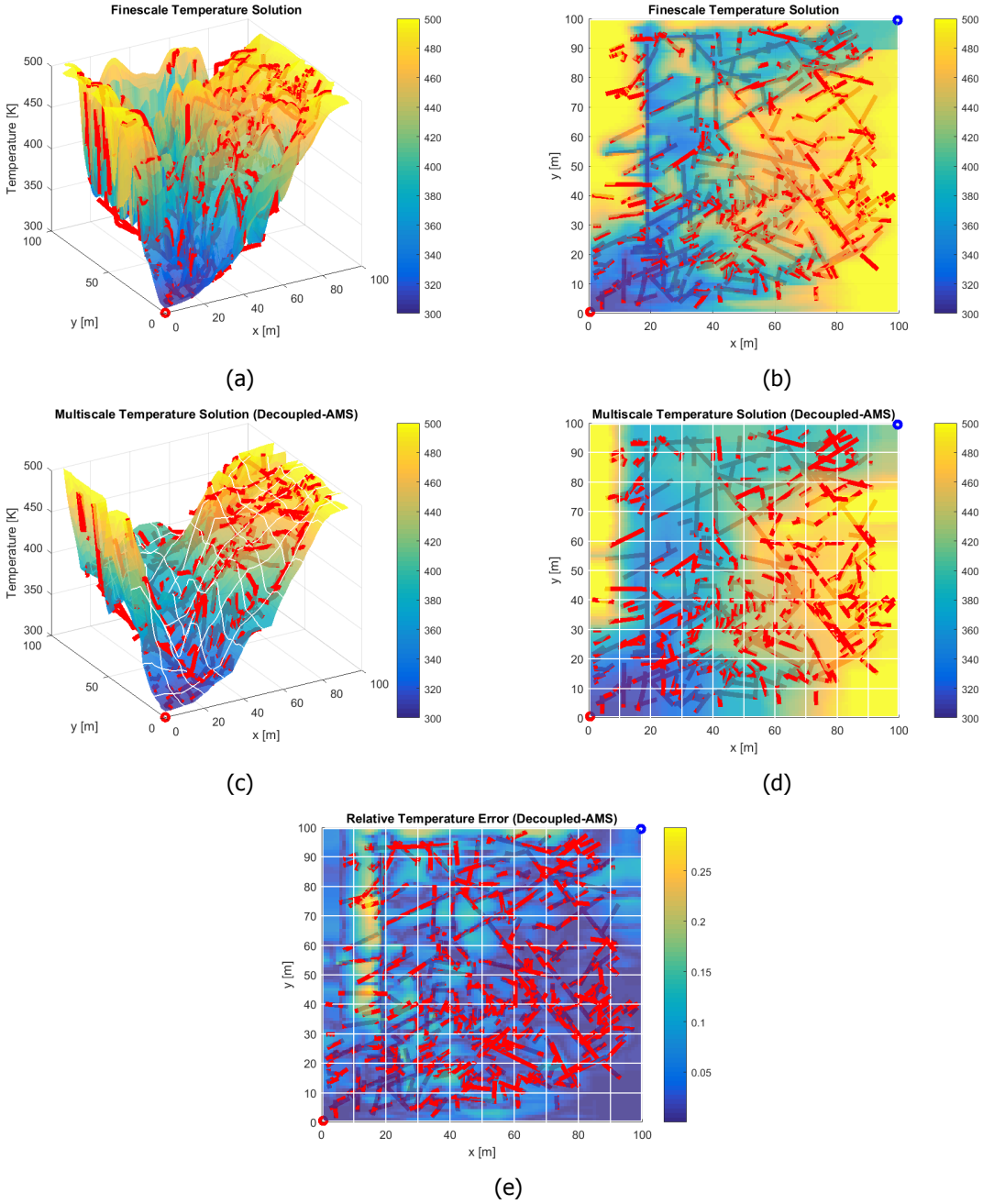

Figure 5.21: Fine-scale (a and b) obtained with 100×100 grid cells and 3860 fracture elements, and multiscale approximate temperature solution obtained using Decoupled-AMS (c and d) in surface plot (left column) and top view (right column) with 10×10 coarse matrix and 386 fracture grid cells at the first iteration stage before smoothing. The corresponding relative error norm (e) is $\|e_T\|_2 = 0.0467$. After 1 stage of smoothing this error reduces to $\|e_T\|_2 = 0.0180$.

5.5. Remarks

Although we employed the MSFV iterations to reach convergence in our sequential implicit framework, one can stop iterations before convergence is reached. The tolerance to stop iterations of a conservative MS solver needs to be defined based on the influence of the solution in the overall accuracy of the coupled solutions, the stability of the time-dependent solutions, and the uncertainty within the parameters. Similar to previous studies for coupled flow and transport [33], such a study is needed for coupled P-T as a future work. Specially, in presence of strong coupling one may consider formulating a multiscale methodology for fully-implicit systems [30, 34].

6

Conclusions

In this research project, a multiscale method for coupled single-phase flow-heat equation in fractured reservoirs was developed. The coupling between the equations was treated by a sequential implicit framework, where both pressure and temperature systems were solved by a multiscale finite volume method. The multiscale formulation was enriched due to the presence of the fractures, with two coupling approaches for local basis functions of each solver. An embedded discrete fracture modeling (EDFM) approach was adapted to the framework, which allows for independent grids for matrix and fractures. This further facilitated the convenient multiscale formulation and implementation, as totally independent coarse grids were also imposed on matrix and fractures. Test cases were performed first to validate the implementation of the simulator (via comparing its results with a DNS approach), and then to systematically assess the performance of the multiscale method for heterogeneous and highly fractured media. A fracture formation from a real-field outcrop was also considered to illustrate the capacity of the algorithm in addressing complex fracture networks.

As for the multiscale basis functions, to exploit the maximum efficiency, the temperature basis function was formulated based on the elliptic part of the energy conservation equation (i.e. the conduction term). Numerical results showed that such an approach is well suited for the considered single-phase fluid-dynamic system, i.e., it leads to accurate results even without smoothing stage.

This work has developed a robust approach to solve for the coupled pressure and temperature equations in fractured heterogeneous reservoirs. The results presented in chapter 5 show promising framework for further developments for field scale enhanced geothermal systems. In view of the author, future developments need to consider the following:

- More relevant complex fluid and rock physics should be included in our framework. To name one for each, the multiphase (including steam) effects for fluid and the geo-mechanical effects (including fracture activations or closures and propagation) for solid rock would be needed to be addressed in future work.
- It is more advantageous to first construct a P-T fully implicit system, and then reduce it to sequential implicit in the case the coupling was weak (like in our case) [34]. Such a general approach would allow for future studies where the coupling could be strong, when more complex fluid and rock physics is considered.
- One should also address a benchmark study based on the CPU time for large-scale systems on a compilable programming language (e.g. C++). Similar to the successful benchmarking of F-AMS [1], such a study for our coupled P-T system is expected to result in more reliable predictions for field-scale applications.

A

Fluid Model

Accurate calculation of fluid properties is needed for accurate pressure and temperature calculation. In this research, the reservoir is assumed to be fully saturated with single phase water (liquid).

All the water properties are calculated using International Association for the Properties of Water and Steam Industrial Formulation 1997 (IAPWS-IF97) [4]. The results are used as the basis for curve fitting to obtain simpler equations with reasonable accuracy. This method is used to maintain the efficiency of fluid properties calculation in the simulator, due to the fact that some of the formulations provided have to be solved iteratively and many of them involve many correlation parameters which might hamper the computational efficiency. These models are simpler and provide continuous data over the whole pressure and temperature interval, therefore eliminating the need of table lookup.

This appendix describes the simplified formulations for calculation of properties needed in the simulation: water saturation properties, density, specific internal energy, and viscosity. Properties obtained from these formulations are compared with data provided by IAPWS-IF97 to validate their accuracy.

A.1. IAPWS-IF97

IAPWS-IF97 is the industry-accepted formulation for calculations of water and steam thermodynamic properties. The formulation is divided into five different regions on which it is valid (see figure A.1).

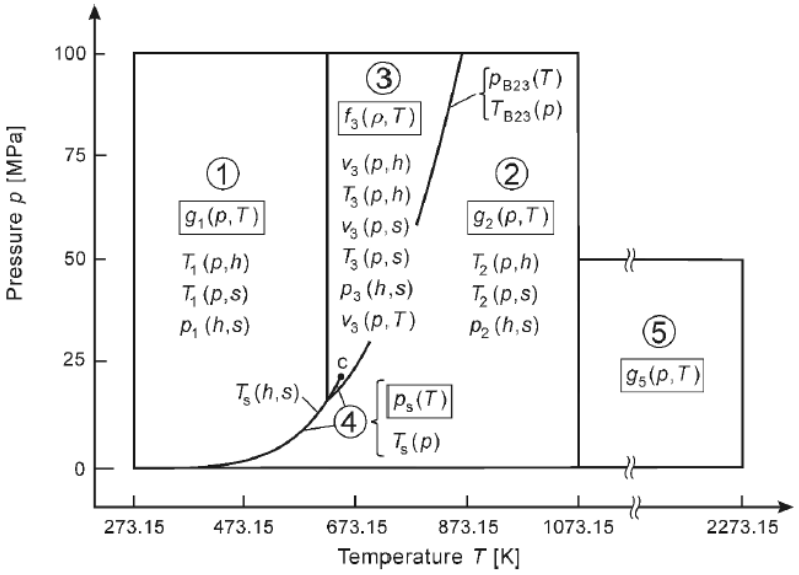

Figure A.1: Regions of IAPWS-IF97 taken from [4].

Region 1 and 2 covers single-phase system, namely liquid and vapour, respectively. Region 3 is near critical as well as supercritical condition, and region 4 is the two-phase region and is used to calculate saturation condition (saturation pressure, temperature, density, internal energy). Region 5 is high-temperature region and is not considered in this thesis work.

A.2. Simplified Fluid Model

Fluid properties such as density and specific internal energy can be defined by a simple correlation between their values at saturation condition and their partial derivative with regards to pressure (compressibility for density calculation) and temperature (specific heat for internal energy calculation) [25], i.e.,

$$\rho_w \cong \rho_{ws}(T)[1 + c_w(T)(p - p_s(T))] \tag{A.1}$$

$$u_w \cong u_{ws}(p) + C_{pw}(p)(T - T_s(p)) \tag{A.2}$$

$$h_w = u_w + \frac{p}{\rho_w} \tag{A.3}$$

Based on these definitions, simplified formulations are needed to calculate saturation properties and isothermal compressibility, c_w, while specific heat, C_{pw}, is assumed to be constant since it does not change significantly for different pressures and temperatures.

A.2.1. Saturation Pressure and Temperature

Based on IAPWS-IF97 [4], parameters used to calculate the saturation pressure is defined as follows:

$$\vartheta = T + \frac{n_9}{T - n_{10}}, \tag{A.4}$$

$$A = \vartheta^2 + n_1\vartheta + n_2, \tag{A.5}$$

$$B = n_3\vartheta^2 + n_4\vartheta + n_5, \text{and} \tag{A.6}$$

$$C = n_6\vartheta^2 + n_7\vartheta + n_8, \tag{A.7}$$

with the empirical parameters, n_i, are shown in table A.1. The saturation pressure, p_s (in Pa), is calculated based on these correlation parameters, i.e.,

$$p_s = \left[\frac{2C}{-B + (B^2 - 4AC)^{0.5}}\right]^4 \times 10^6, \tag{A.8}$$

with the validity ranging from $273.15\ K \leq T \leq 647.096\ K$ (critical point).

Parameters used in saturation temperature calculation are calculated as follows:

$$\beta = \left(\frac{p}{10^6}\right)^{0.25}, \tag{A.9}$$

$$E = \beta^2 + n_3\beta + n_6, \tag{A.10}$$

Table A.1: Coefficients of correlation for saturation pressure and temperature calculation from [4].

i	n_i	i	n_i
1	$0.116\ 705\ 214\ 527\ 67 \times 10^4$	6	$0.149\ 151\ 086\ 135\ 30 \times 10^2$
2	$-0.724\ 213\ 167\ 032\ 06 \times 10^6$	7	$-0.482\ 326\ 573\ 615\ 91 \times 10^4$
3	$-0.170\ 738\ 469\ 400\ 92 \times 10^2$	8	$0.405\ 113\ 405\ 420\ 57 \times 10^6$
4	$0.120\ 208\ 247\ 024\ 70 \times 10^5$	9	$-0.238\ 555\ 575\ 678\ 49$
5	$-0.323\ 255\ 503\ 223\ 33 \times 10^7$	10	$0.650\ 175\ 348\ 447\ 98 \times 10^3$

$$F = n_1\beta^2 + n_4\beta + n_7\,, \text{and} \tag{A.11}$$

$$G = n_2\beta^2 + n_5\beta + n_8\,, \tag{A.12}$$

with the empirical parameters, n_i, are also shown in table A.1. The saturation temperature, T_s (in K), is calculated based on these correlation parameters, i.e.,

$$T_s = \frac{2G}{-F + (F^2 - 4EG)^{0.5}}\,, \tag{A.13}$$

with the validity ranging from $611.2\ Pa \leq p \leq 22.064\ MPa$ (critical point).

For these properties, no simplified models are developed due to the fact that the equations provided in IAPWS-IF97 are not complex. Both saturation pressure and temperature are plotted in figure A.2.

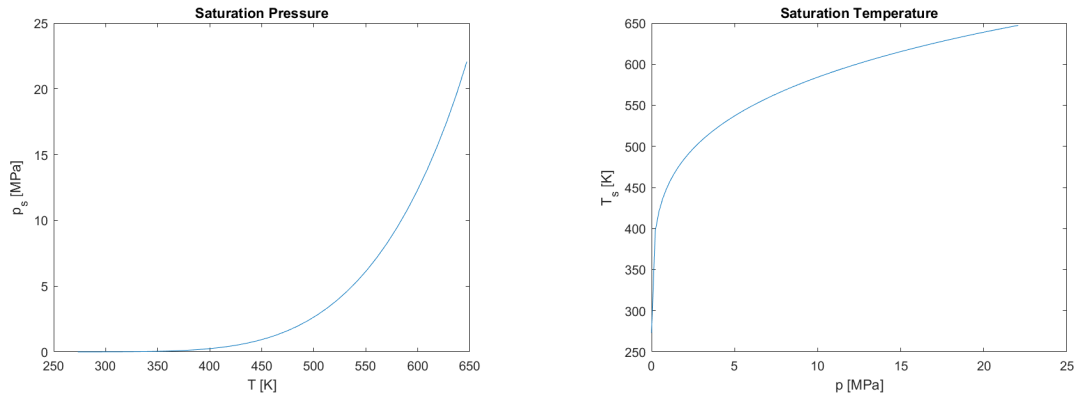

(a) (b)

Figure A.2: Saturation pressure (a) and saturation temperature (b).

A.2.2. Density

Saturation density and compressibility data are needed to calculate water density, as well as saturation pressure which is used as the reference pressure. A curve fitted equation is used to match the density at saturation condition with data from steam table. The simplified equation used in the curve fitting is

$$\rho_{ws} = \begin{cases} -0.0032\ T^2 + 1.7508\ T + 757.5, & \text{for } T \leq 623.15\ K \\ -0.5214\ T^2 + 652.73\ T - 203714, & \text{for } T > 623.15\ K \end{cases}. \tag{A.14}$$

The isothermal compressibility values are back-calculated from the water density at different pressures and temperatures, saturation density, and saturation pressure using equation A.1, i.e.,

$$c_w = (0.0839T^2 - 64.593T + 12437) \times 10^{-12}, \text{for } 273\ K < T < 647\ K\,. \tag{A.15}$$

Water densities at various pressures and temperatures are calculated using simplified model and are compared with empirical data from IAPWS-IF97, shown in figure A.3. Notice that the difference between both results are small enough and therefore, this simplified model is proven to be a good approximation for the water density. The relative error norm obtained from the simplified model is below 1%, with slightly higher error norm of 2.2 % near critical point. It also proves that the simplified model is valid to be used at $273.15\ K \leq T \leq 647.096\ K$ and $p_s(T) \leq p \leq 22.064\ MPa$, which is the single phase liquid region. The fact that water is slightly compressible also makes the approximation reasonable.

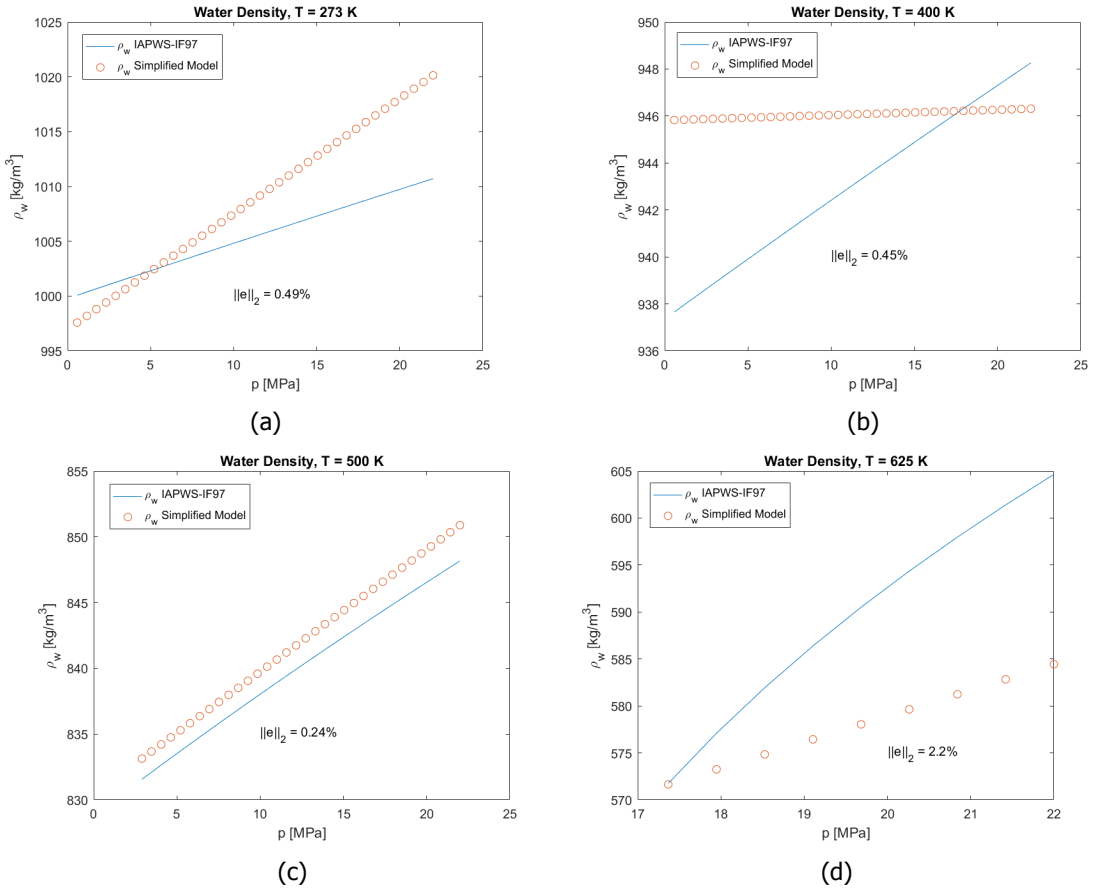

Figure A.3: Comparison of water density calculated with simplified model and IAPWS-IF97 at: 273 K (a), 400 K (b), 500 K (c), and 625 K (d).

A.2.3. Specific Internal Energy

Saturation specific internal energy and specific heat data are needed to calculate water specific internal energy, as well as saturation temperature which is used as the reference temperature. It is found that using constant saturation properties: specific internal energy at saturation condition, specific heat, and saturation temperature leads to better approximation. The combination of $u_{ws} = 420,000\ J/kg$, $C_{pw} = 4,200\ J/kg$, and $T_s = 373\ K$ give best fit to the empirical data. Figure A.4 shows the comparison between the data obtained from the calculation with the simplified model using constant saturation properties and empirical data obtained using IAPWS-IF97. The match between both data is extremely good, with the relative error norm less than 6%. The error is also more pronounced near the critical point, but the relative error norm is still reasonably low. Together with pressure and density, these specific internal energy values are used to calculate the specific enthalpy as described in equation A.3.

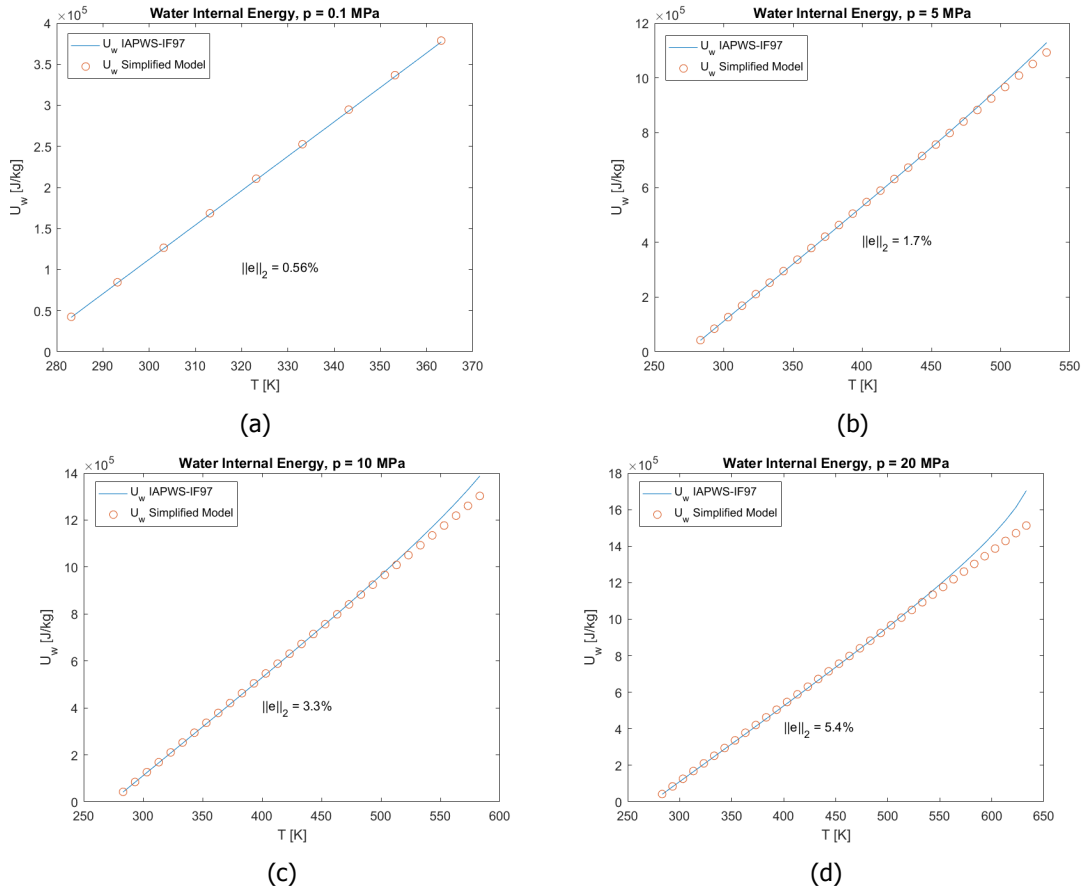

Figure A.4: Water specific internal energy calculated with simplified model (constant saturation properties) and IAPWS-IF97 at: 0.1 MPa (a), 5 MPa (b), 10 MPa (c), and 20 MPa (d).

A.2.4. Viscosity

In simulations with isothermal assumption, viscosity is always assumed to be constant. In geothermal simulations, however, temperature plays an important role to viscosity. The viscosity-temperature relationship is given by [35]

$$\mu_w = 2.414 \times 10^{-5} \times 10^{\frac{247.8}{T-140}}. \tag{A.16}$$

Bibliography

[1] M. Tene, M. S. A. Kobaisi, and H. Hajibeygi, *Algebraic multiscale method for flow in heterogeneous porous media with embedded discrete fractures (F-AMS),* in *Journal of Computational Physics*, Vol. 321 (2016) pp. 819–845.

[2] H. Hajibeygi, D. Karvounis, and P. Jenny, *A hierarchical fracture model for the iterative multiscale finite volume method,* in *Journal of Computational Physics*, Vol. 230 (2011) pp. 8729–8743.

[3] K. Bisdom, B. Gauthier, G. Bertotti, and N. Hardebol, *Calibrating discrete fracture-network models with a carbonate three-dimensional outcrop fracture network: Implications for naturally fractured reservoir modeling,* in *AAPG Bulletin*, Vol. 98 (2014) p. 1351–1376.

[4] W. Wagner and H.-J. Kretzschmar, *International Steam Tables - Properties of Water and Steam based on the Industrial Formulation IAPWS-IF97*, 2nd ed. (Springer, 2008).

[5] UNFCCC, *Paris Agreement,* (2016).

[6] J. G. Olivier, G. Janssens-Maenhout, M. Muntean, and J. A. Peters, *Trends in Global CO_2 Emissions 2016 Report*, Tech. Rep. (PBL Netherlands Environmental Assessment Agency, 2016).

[7] MIT, *The Future of Geothermal Energy - Impact of Enhanced Geothermal Systems (EGS) on the United States in the 21^{st} Century,* (2006).

[8] B. Matek, *2016 Annual US & Global Geothermal Power Production Report*, Tech. Rep. (Geothermal Energy Association, 2016).

[9] M. W. McClure, *Fracture Stimulation in Enhanced Geothermal Systems*, MSc thesis, Stanford University (2009).

[10] J. Warren and P. Root, *The Behavior of Naturally Fractured Reservoirs,* in *SPE Journal*, Vol. 3 (1963) pp. 245–255.

[11] M. Karimi-Fard, L. Durlofsky, and K. Aziz, *An Efficient Discrete-Fracture Model Applicable for General-Purpose Reservoir Simulators,* in *SPE Journal* (2004) pp. 227–236.

[12] L. Li and S. H. Lee, *Efficient Field-Scale Simulation of Black Oil in Naturally Fractured Reservoir Through Discrete Fracture Networks and Homogenized Media,* SPE Reservoir Evaluation and Engineering , 750 (2008).

[13] S. Lee, M. Lough, and C. Jensen, *Hierarchical modeling of flow in naturally fractured formations with multiple length scales,* Water Resource Research **37**, 443 (2001).

[14] A. Moinfar, W. Narr, M.-H. Hui, B. Mallison, and S. H. Lee, *Comparison of Discrete-Fracture and Dual-Permeability Models for Multiphase Flow in Naturally Fractured Reservoirs,* in *SPE Reservoir Simulation Symposium* (Society of Petroleum Engineers, 2011).

[15] S. Pluimers, *Hierarchical Fracture Modeling Approach*, MSc thesis, Delft University of Technology, The Netherlands (2015).

[16] J. H. Norbeck, M. W. McClure, J. W. Lo, and R. N. Horne, *An embedded fracture modeling framework for simulation of hydraulic fracturing and shear stimulation,* in *Computational Geosciences*, Vol. 20 (2016) pp. 1–18.

[17] P. Jenny, S. Lee, and H. Tchelepi, *Multi-scale finite-volume method for elliptic problems in subsurface flow simulation,* in *Journal of Computational Physics*, Vol. 187 (2003) pp. 47–67.

[18] I. Lunati and S. H. Lee, *An Operator Formulation of the Multiscale Finite-Volume Method with Correction Function,* in *Multiscale Modeling and Simulation*, Vol. 8 (2009) pp. 96–109.

[19] H. Zhou and H. Tchelepi, *Operator-Based Multiscale Method for Compressible Flow,* in *SPE Journal* (2008) pp. 267–273.

[20] H. Hajibeygi, G. Bonfigli, M. A. Hesse, and P. Jenny, *Iterative multiscale finite-volume method,* in *Journal of Computational Physics*, Vol. 227 (2008) pp. 8604–8621.

[21] H. Hajibeygi and P. Jenny, *Multiscale finite-volume method for parabolic problems arising from compressible multiphase flow in porous media,* in *Journal of Computational Physics*, Vol. 228 (2009) pp. 5129–5147.

[22] M. Tene, Y. Wang, and H. Hajibeygi, *Adaptive algebraic multiscale solver for compressible flow in heterogeneous porous media,* in *Journal of Computational Physics*, Vol. 300 (2015) pp. 679–694.

[23] S. M. HosseiniMehr, *Multilevel Multiscale Method for Embedded Discrete Fracture Modeling Approach (F-MLMS)*, MSc thesis, Delft University of Technology, The Netherlands (2016).

[24] D. W. Peaceman, *Interpretation of Well-Block Pressures in Numerical Reservoir Simulation,* in *SPE-AIME Annual Fall Technical Conference and Exhibition* (Denver, Colorado, 1977).

[25] K. H. Coats, *Geothermal Reservoir Modelling,* in *SPE Annual Fall Technical Conference and Exhibition* (Denver, Colorado, 1977).

[26] V. Lampe, *Modelling Fluid Flow and Heat Transport in Fractured Porous Media*, Master's thesis, University of Bergen (2013).

[27] M. C. Suárez-Arriaga, *Local Thermal Non-Equilibrium Interfacial Interactions in Heterogeneous Reservoirs - Divergence of Numerical Methods to Simulate the Fluid and Heat Flow,* in *40th Workshop on Geothermal Reservoir Engineering* (Stanford University, Stanford, California, 2016).

[28] H. K. Versteeg and W. Malalasekera, *An Introduction to Computational Fluid Dynamics: The Finite Volume Method,* (Pearson Education Limited, 2007) Chap. 5, 2nd ed.

[29] A. Marelis, *Energy capacity of a geothermal reservoir: The effect of conductive heat transfer recharge on reservoir lifetime at low temperature conduction regimes*, BSc thesis, Delft University of Technology, The Netherlands (2017).

[30] Z. Y. Wong, R. Rin, H. Tchelepi, and R. Horne, *Comparison of Fully Implicit and Sequential Implicit Formulation for Geothermal Reservoir Simulations,* in *42nd Workshop on Geothermal Reservoir Engineering* (Stanford University, Stanford, California, 2017).

[31] Y. Saad, *Iterative Methods for Sparse Linear Systems*, 2nd ed. (Society for Industrial and Applied Mathematics, 2003).

[32] M. Tene, S. Bosma, M. A. Kobaisi, and H. Hajibeygi, *Projection-based Embedded Discrete Fracture Model (pEDFM),* in *Advances in Water Resources*, Vol. 105 (2017) pp. 205–216.

[33] H. Hajibeygi, S. Lee, and I. Lunati, *Accurate and Efficient Simulation of Multiphase Flow in a Heterogeneous Reservoir With Error Estimate and Control in the Multiscale Finite-Volume Framework,* in *SPE Journal*, Vol. 17 (2012) pp. 1071–1083.

[34] M. Cusini, C. van Kruijsdijk, and H. Hajibeygi, *Algebraic dynamic multilevel (ADM) method for fully implicit simulations of multiphase flow in porous media,* in *Journal of Computational Physics*, Vol. 314 (2016) pp. 60–79.

[35] P. T. Al-Shemmeri, *Engineering Fluid Mechanics,* (Bookboon, 2012) Chap. 1, p. 18.

[36] M. A. Grant and P. F. Bixley, *Geothermal Reservoir Engineering*, 2nd ed. (Elsevier Inc., 2011).

[37] T. D. Eastop and A. McConkey, *Applied Thermodynamics for Engineering Technologists,* (Longman Scientific & Technical, 1993) Chap. 16, 5th ed.

[38] I. Lunati and P. Jenny, *Multiscale finite-volume method for compressible multiphase flow in porous media,* in *Journal of Computational Physics*, Vol. 216 (2006) pp. 616–636.

[39] Y. Wang, H. Hajibeygi, and H. A. Tchelepi, *Algebraic multiscale solver for flow in heterogeneous porous media,* in *Journal of Computational Physics*, Vol. 259 (2014) pp. 284–303.

[40] H. Tchelepi, P. Jenny, S. Lee, and C. Wolfsteiner, *Adaptive Multiscale Finite-Volume Framework for Reservoir Simulation,* in *SPE Journal* (2007) pp. 188–195.

[41] Y. Efendiev, T. Hou, and V. Ginting, *Multiscale Finite Element Methods for Nonlinear Problems and Their Applications,* in *Communications in Mathematical Sciences*, Vol. 2 (2004) pp. 553–589.

[42] A. R. Shaik, S. S. Rahman, N. H. Tran, and T. Tran, *Numerical simulation of Fluid-Rock coupling heat transfer in naturally fractured geothermal system,* in *Applied Thermal Engineering*, Vol. 31 (2011) pp. 1600–1606.

[43] Y. Hao, P. Fu, and C. R. Carrigan, *Application of a Dual-Continuum Model for Simulation of Fluid Flow and Heat Transfer in Fractured Geothermal Reservoirs,* in *38th Workshop on Geothermal Reservoir Engineering* (Stanford University, Stanford, California, 2013).

[44] Y. Wang, H. Hajibeygi, and H. A. Tchelepi, *Monotone multiscale finite volume method,* in *Computational Geosciences*, Vol. 20 (2015) pp. 509–524.

[45] BP, *BP Statistical Review of World Energy 2017*, Tech. Rep. (BP, 2017).

[46] J. W. Lund, *100 Years of Geothermal Power Production,* in *30th Workshop on Geothermal Reservoir Engineering* (Stanford University, Stanford, California, 2005).